The Effect of Material Properties on Energy Resolution in

Gamma-ray Detectors

by

Raman Narayan

A Dissertation Presented in Partial Fulfillment
of the Requirements for the Degree
Doctor of Philosophy

Approved March 2011 by the
Graduate Supervisory Committee:

Peter Rez, Chair
John Spence
Fernando Ponce
Joseph Comfort
Andrew Chizmeshya

ARIZONA STATE UNIVERSITY

May 2011

ABSTRACT

Nuclear proliferation concerns have resulted in a desire for radiation detectors with superior energy resolution. In this dissertation a Monte Carlo code is developed for calculating energy resolution in gamma-ray detector materials. The effects of basic material properties such as the bandgap and plasmon resonance energy are studied using a model for inelastic electron scattering based on electron energy-loss spectra. From a simplified "toy model" for a generic material, energy resolution is found to oscillate as the plasmon resonance energy is increased, and energy resolution can also depend on the valence band width. By incorporating the model developed here as an extension of the radiation transport code Penelope, photon processes are also included. The enhanced version of Penelope is used to calculate the Fano factor and average electron-hole pair energy in semiconductors silicon, gallium arsenide, zinc telluride, and scintillators cerium fluoride and lutetium oxyorthosilicate (LSO). If the effects of the valence band density-of-states and phonon scattering are removed, the calculated energy-resolution for these materials is fairly close to that for a toy model with a uniform electron energy-loss probability density function. This implies that the details of the electron cascade may in some cases have only a marginal effect on energy resolution.

ACKNOWLEDGMENTS

TABLE OF CONTENTS

LIST OF TABLES

LIST OF FIGURES

1   Introduction

National security concerns have provided motivation for the development of radiation detectors that are capable of gamma-ray spectroscopy, in addition to spectroscopy for other radioactive decay particles which include alpha particles and neutrons. The International Atomic Energy Agency (IAEA) has reported 18 incidents involving the smuggling of weapons grade nuclear materials (uranium-235 and plutonium-239) from 1993 to 2004. There have been many more attempts to smuggle other nuclear isotopes, such as americium-241, californium-252, cesium-137, cobalt-60, iridium-192, and strontium-90, that could be used to produce a "dirty bomb"[1]. Since the 9/11 terrorist attacks, these concerns have become all the more urgent.

     In addition to working with foreign governments (such as the Russians and former Soviet bloc countries) to secure nuclear materials, the US government has installed radiation detection equipment at shipping ports and ports of entry both in the US and abroad[1]. In addition to merely detecting radioactivity, it is advantageous to be able to measure the energy of decay products. Harmless cargo, such as medical isotopes and kitty litter, could set off false alarms which might make a radiological monitoring system unfeasible[1]. In this dissertation, the production of electron-hole pairs due to ionizing radiation is studied in the context of energy resolution in gamma-ray detector materials.

     Gamma-ray spectra from several elements are shown in Figure 1 which is taken from [1]. The energy range of interest for special nuclear material, that is, uranium-235 and plutonium-239, is in the 150 – 500 keV range. The general

issue of the detectability of specific materials in realistic scenarios involves the

geometries of sources, detectors, and the separation of particular features in the

gamma-ray spectrum and radiological background. One also must consider

interactions with any solid or liquid that lies between the source and the detector,

which includes the issue of an advanced "evil-doer" who masks the nuclear

material with lead shielding or commonplace cargo (like kitty litter, etc.) that is

also radioactive[1]. These concerns are outside the scope of this work. Here the

focus is on how the properties of gamma-ray detector materials affect the statistics

of electron-hole pair production. This determines the best possible energy

resolution that could be obtained for mono-energetic gamma-rays.   In the

remainder of this introduction, some background information and previous work
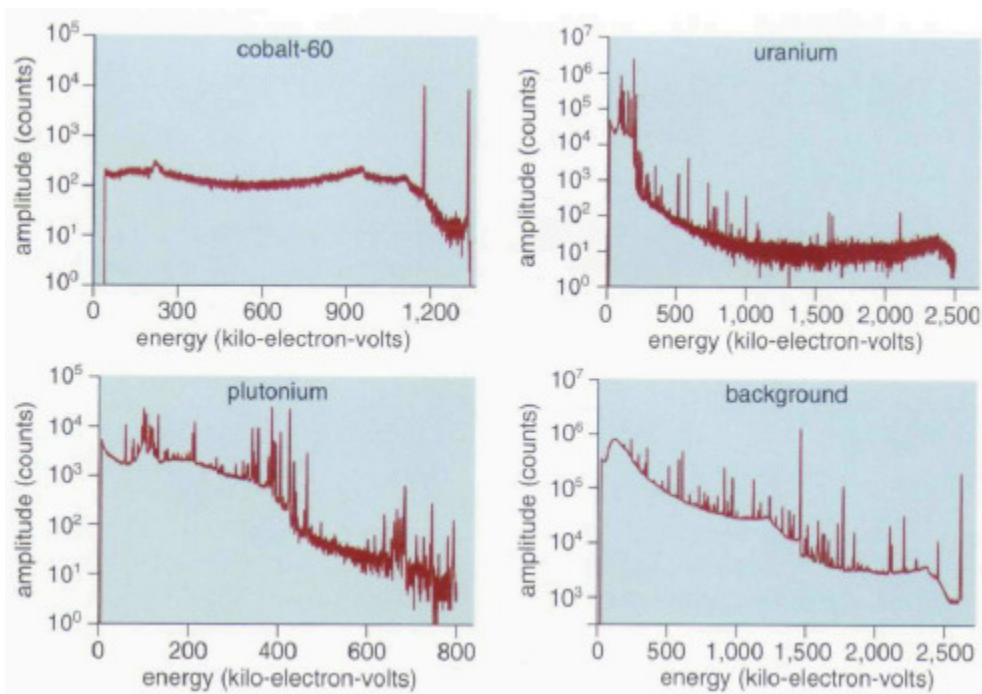
Figure 1. Gamma ray spectra from cobalt-60, uranium, plutonium, and the radioactive background that would compete signals with these in a practical application.

in this field will be discussed, and then the organization of this dissertation is outlined.

After a gamma-ray ($<1\,\mathrm{MeV}$) enters the detector material, its first interaction will be either Compton scattering or photoelectric absorption. In both cases high energy (keV) electrons will be generated. The lower energy photons resulting from the initial Compton scattering will either undergo more Compton scattering or photoelectric ionization events. Both of these processes, as well as inelastic electron scattering, can result in vacancies in the inner atomic shells. Additional X-rays and Auger electrons result from the relaxation cascade of these vacancies. These interactions culminate in a number of fast electrons, which produce further ionization, and hence a cascade of electrons. A conceptual diagram of the initial interactions for a gamma-ray is shown in Figure 2. The subsequent thermalization of the electron cascade culminates in the distribution of electron-hole pairs that constitutes the detector response. Although the initial photon processes are of practical concern in the design of detectors, it is ultimately the cascade process that begins with fast electrons which will determine energy resolution. For a scintillation counter, electrons and holes migrate to impurity (or intrinsic) metastable states and then recombine, producing scintillation photons. These photons are recorded by some kind of photodetector – usually a photomultiplier tube (PMT)[2]. In a semiconductor detector, the electrons and holes are swept towards opposite electrical contacts by a strong bias voltage[2]. In either case, the statistics that govern the production of electron hole pairs, or information carriers, sets a best-case limit for the energy resolution.
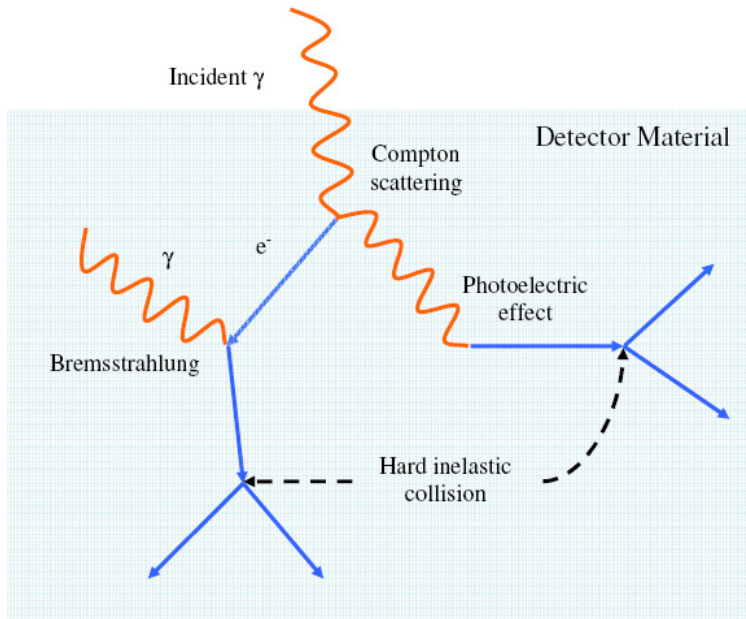
Figure 2. Schematic picture of initial scattering events inside a gamma ray detector.

The first study of the statistics of information carrier production in radiation detectors is probably that of Fano[3] in 1947, who was interested in the energy-resolution in ionization chambers. He introduced the *Fano Factor* (*F*) (§3.1) which is defined as the sample variance in the number of information carriers produced by an incident particle divided by the expected number of information carriers (the variance given by Poisson statistics). Since then a number of researchers have studied the statistics of cascade processes.

The first published model called "crazy carpentry" by its author[4] involved randomly distributing electron energy into two parts and then subtracting a unit equivalent to the band gap energy from the smaller of the two fractions. The process was continued with both of the fractions until it could no longer be repeated. This model took account of the band gap but did not consider any variation in the densities of states. Subsequent developments by Alig[5] assumed

4

that the electron energy was distributed between valence electron excitation and optic phonons. Parabolic free electron densities of states were assumed for both valence and conduction bands. A solution to a recursive master equation describing the process was used to estimate the expected variance for various semiconductor detectors. In a subsequent paper, a Monte Carlo scheme was used for the calculation of variance[6].

More recently, Fraser et al.[7] used a Monte Carlo calculation to derive the Fano factor for X-rays incident on a silicon CCD detector used in an X-ray telescope. Their treatment was more comprehensive in that it incorporated all of the relevant scattering processes, but less so in that details of the valence band structure were neglected. Gao et al. followed up on Fraser's work and produced an improved code with results for Si[8] and Ge[9]. Devanathan et al.[10] published a review of issues affecting energy resolution in different types of detectors, and a theory by Jordan[11] reduced the problem of electron-hole pair generation to taking variably-sized "shots" from a finite bathtub. Recently Caleman et al.[12, 13] have performed calculations of the secondary electron cascade both for photocathode materials such as KI and CsI, and organic materials, to investigate how materials behave when subjected to intense femtosecond X-ray pulses. An electron loss function derived from calculated band structures that included a self-energy correction was used in their simulation.

These studies have been supported by advances in the understanding of inelastic scattering for low energy electrons. Kane[14] was the first to use computed band structures to calculate low energy inelastic scattering and electron

hole pair production in silicon. Sano and Yoshii[15] calculated ionization thresholds and probabilities in addition to other related quantities for conduction-band electrons in silicon, with an emphasis on the effect of anisotropy in wave-vector dependence.

In this dissertation we introduce a Monte Carlo scheme that explicitly calculates the number of electron-hole pairs due to electron inelastic scattering. Calculating the differential cross section from first principles theory following Caleman[12, 13], is very time consuming and can only be done over a limited range of energies. Instead we take the measured transmission electron energy loss spectrum as a convenient measure of the direct differential scattering cross section. This means that our procedure is applicable to a wide range of potential detector materials and is not limited to elemental semiconductors. Though in principle similar to Alig[6] and Fraser[7], the important differences are, respectively, the use of a differential cross-section (DCS) based on scattering physics rather than an assumption of uniform probability, and a more realistic treatment of plasmon decay and holes. This inelastic scattering model is integrated into the Penelope radiation transport code[16], which allows one to simulate photon processes as well. The modified Penelope code will be used for the calculation of the Fano factor and energy resolution for gamma-rays in different materials.

In the following chapter some background information is given for different types of radiation detectors. In §3 issues of overall detector energy resolution are discussed. §4 contains the physics of the inelastic scattering

6

processes considered here, the development of the electron cascade, and results where only inelastic electron scattering is considered. In §5 photon scattering processes are summarized, as is the utilization of the Penelope radiation transfer code. The implementation of the complete model for specific materials is described in detail in §6 and results are shown. Finally, there is a discussion of results and remaining issues (§7) and conclusions (§8).

2   Gamma-ray detector background

Most radiation detectors fit into three categories according to the media they use for converting the energy of incident radiation into information carriers. These are gas-filled detectors, scintillation counters, and semiconductor diode detectors.

2.1   Gas detectors

A gas filled radiation detector has a chamber filled with gas that is ionized by the incident radiation. A cathode and anode provide an electric field to collect the resulting electrons and ions. Different types of gas detectors have chambers with different geometries and operate in different ways. The d.c. ionization chamber, pulse ionization chambers, proportional counters, and Geiger counters are discussed below. Due to the relatively long range of higher energy electrons and photons in gasses, only a fraction of such a particle's energy will be deposited in the chamber making gas detectors impractical for obtaining their energy spectra. Gas chambers must be filled with gasses that will not readily take on electrons (such as the noble gasses), or in the case of proportional and Geiger counters, produce unwanted feedbacks[2]. Although ionization potentials vary, particles suffer an average loss of about $35\,\mathrm{eV}$ per ionization in commonly used gasses.[17]

A d.c. ionization chamber is bounded on two sides by parallel capacitor plates, and insulating walls on the remaining sides. The properties of these walls can be important, since their interaction with radiation can result in additional electrons in the chamber. The capacitor plates are connected to a steady voltage source and changes in current due to the collection of electrons and ions can be

measured to define the pulse. These devices are usually used to monitor

continuous gamma backgrounds.[2]

By allowing the above capacitor to discharge when the gas is ionized, one

can measure the pulse using the drop in voltage across the capacitor. This is the

idea behind the pulse ionization chamber. An idealized diagram is shown in

Figure 3. The capacitor is charged to voltage V_0 when the switch S is closed.

When S is open, changes in voltage due to ionization can be measured. One must

keep in mind that the pulse is affected by the location of the ionization track in the

chamber since electrons have much higher mobility than ions. Spectroscopy is

possible for alpha particles. A 5 MeV alpha particle, for example, could be

resolved to 0.02 MeV.[2]
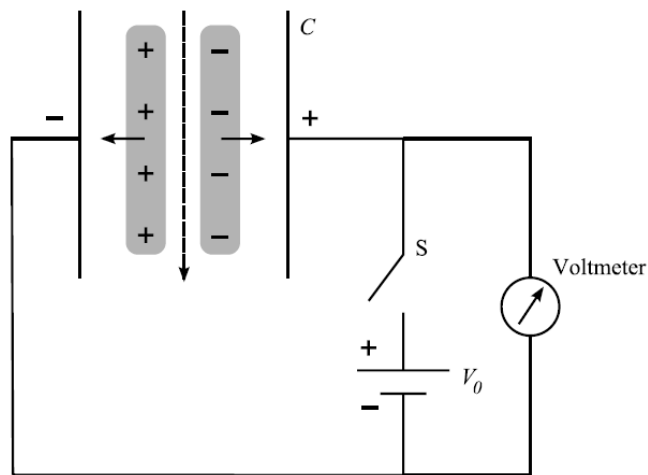
Figure 3. Idealized pulse ionization chamber (from Delaney and Finch 1992).

If the field in the ionization chamber is sufficiently high, electrons

produced by ionizing radiation can ionize other atoms or molecules, which

reduces the amount of external amplification required. In a proportional counter,

as its name implies, the number of electrons and ions after multiplication is

9

proportional to the energy of the incident radiation particle, making spectrometry possible for radiation that deposits its entire energy in the detector. A common geometry for such a device is a cylindrical cathode and an anode that is a wire along the cylinder's axis. Since the electric field in this geometry is inversely proportional to the distance from the anode wire, most ionization occurs when electrons get very close (within ~10 μm) to the anode wire. It is therefore usually not important where the initial ionization occurs. The full pulse may be recorded in milliseconds, although this time can be reduced by a few orders of magnitude if one is willing to settle for only a fraction of the pulse.[2]

When the potential in the proportional counter is further increased multiplication increases to where so many ions are created near the anode that a shielding effect occurs which prevents further multiplication. Now there can be changes in voltage without the multiplication being affected, as illustrated in Figure 4. This is called the "Geiger region" as it is where Geiger counters operate. For a Geiger counter, a single ionization will produce the same signal as many initial ionizations, which makes them useless for spectroscopy. The pressure inside a Geiger counter can be reduced in order to increase carrier mobility and therefore multiplication so that the voltage may be lowered. Geiger counters have the advantages of portability and that they do not require a stable voltage source.[2]
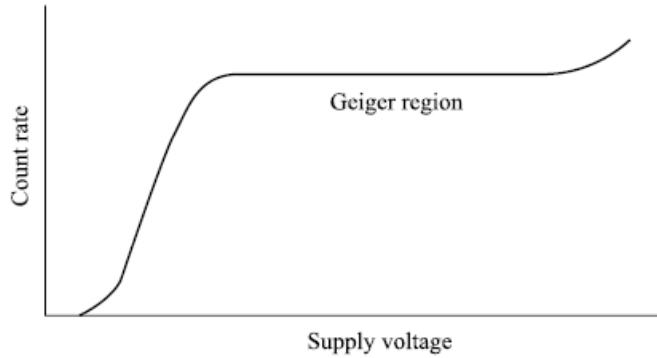
Figure 4. Schematic plot of Geiger region (from Delaney and Finch 1992).

2.2   Scintillation counters

Scintillator materials convert a significant fraction of the energy of incoming radiation to visible or near UV light. This is converted to an electronic signal using a photodetector which is often a photomultiplier tube. There are different types of scintillator materials, which convert energy to light in different ways.

Inorganic scintillators are crystalline solids that often need an activator atom in order to function[2]. A commonly used example is sodium iodide activated with thallium, NaI(Tl). In inorganic scintillators, a significant amount of the energy deposited by the incident radiation is converted to electron hole pairs, and photons are produced when these recombine. The activator atom creates a different pathway for this deexcitation by producing additional states in the scintillator's bandgap, reducing the energy of emitted photons thereby lowering the chance that they will be reabsorbed in the crystal. A schematic illustration of deexcitation in NaI(Tl) is shown in Figure 5. Inorganic scintillators usually have decay times around a microsecond.

11
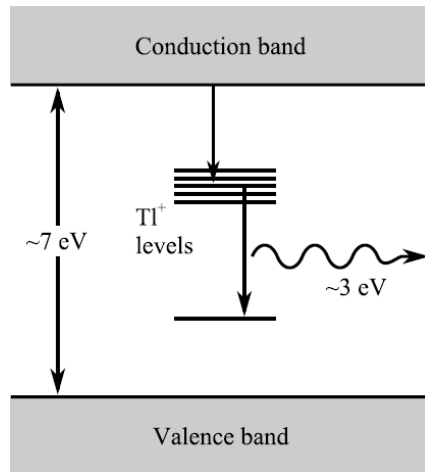
Figure 5. Deexitation process in NaI(Tl) (from Delaney and Finch 1992).

Organic scintillators consist of organic molecules which can be in

crystalline form or suspended in a liquid or plastic. These molecules are aromatic

hydrocarbons that have electronic modes which can be excited by energy

deposited by the incident radiation. There are also more closely spaced vibrational

modes superimposed on the electronic modes. Photons are released when excited

molecules return to their ground electronic states. Anthracene and stilbene are

common examples of the crystalline organics and terphenyl is often used with

liquids or plastics. These organic molecules are shown in Figure 6. Organic

scintillators can have decay times as short as a few nanoseconds ― better than

two orders of magnitude less than those of inorganic scintillators. Organic

scintillators in liquid or plastic can be used to build very large detectors, since

preserving the crystal structure is not a concern. Since they lack heavy elements,

organic scintillators are not efficient at absorbing gamma-radiation. Organic

scintillators are then required to be larger, which complicates the process of the

12

photons reaching the photomultiplier tube, making them generally less efficient than inorganic scintillators.[2, 17]
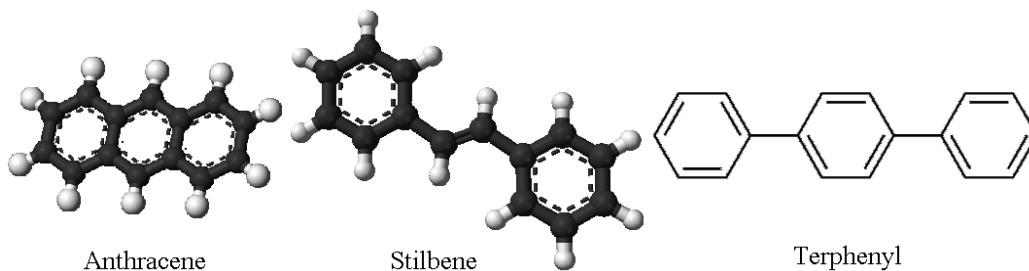
Figure 6. Common organic scintillators. Ball-and-stick models of anthracene and stilbene and skeletal model of terphenyl.

The output pulse of a scintillator can be recorded by a photomultiplier tube in two distinct ways, which are know as "voltage" (or "charge") mode and "current" mode. In voltage mode the total charge output from the photomultiplier is measured for the entire pulse, whereas in current mode the instantaneous current is measured. The former is best for determining energy whereas the latter can be used to measure the pulse shape. It is also possible (though not necessarily practical) to operate a photomultiplier in both modes simultaneously.[2]

2.3 Semiconductor detectors

Semiconductors currently provide superior resolution for spectral features compared to gas detectors or scintillators. Since semiconductors have bandgaps of a few eV or less, significantly less energy is required to produce an electron-hole pair compared to a scintillator, and up to ~ 10 times less than a single ionization in a gas detector. This means a potentially higher number of counts and, assuming Poisson-like statistics, better energy resolution in the case where the incident particle deposits all of its energy, and charge collection is efficient.

13

That charge carriers resulting from ionizing radiation are recorded directly without relying on a photocathode is currently an important advantage over scintillators. Energy resolution may degraded, though, by leakage (dark) current and damage caused by radiation.[2]

Semiconductor detectors are limited to small sizes because defects in the crystalline lattice would otherwise inhibit satisfactory charge collection. Defects, impurities and thermal excitations of electrons across the band gap give semiconductors finite resistivity. The high electric fields that are applied for effective charge collection would then result in currents that could easily swamp any signal from the incident radiation. This is prevented by doping the detector material to create reverse-biased p–n junctions, which may be done in several ways[2, 17, 18].

Silicon and germanium are often used for detectors because their charge transport properties allow for efficient collection of electrons and holes. Electrons and holes can have lifetimes of ms compared to µs in other semiconductors[2]. Since these materials have narrow minimum bandgaps – 1.11 eV for silicon and 0.66 eV for germanium at room temperature, they must in many cases be cooled to suppress thermal excitation of electrons, which would produce an unacceptable amount of dark current[19]. Although germanium requires more cooling than silicon, High Purity Germanium (HPGe) can be manufactured with impurity levels of 1 part in 10^{12}, making possible detectors up to several centimeters thick. Along with its higher stopping power (see §5) this makes for a substantial advantage over silicon in gamma-ray spectroscopy[17]. For electrons, X-rays,

and lower-energy gammas where size and stopping power are less important, silicon can be advantageous in that its larger bandgap causes less leakage current.[18]

Although Si and Ge are the most commonly used semiconductor detector materials, there also exist a number of compound semiconductors materials. Some examples which are commercially available are CdTe, $Cd_{1-x}Zn_xTe$ (CZT), and HgI_2. Compared to Si and Ge these materials have the advantages of higher stopping power and greater bandgaps. The latter is important in that it allows operation at room temperature which makes a detector more economical. The charge transport properties of compound semiconductors are currently inferior compared to Si and Ge, which limits these materials to small sizes.[18]

3 Detector energy resolution

Since we are interested in identifying radioactive materials by measuring the characteristic radiation from their decay, energy resolution is the main criteria in determining the quality of a particular detector material. *Fractional resolution* is defined as $\Delta E/E$ where ΔE is a measure of the typical deviation from the expected energy E of the measured radiation. ΔE is usually defined as the *full width at half maximum* (FWHM) of the peak in question in the energy spectrum. After a general discussion of the statistics of information carriers in detector materials (§3.1), the specific cases of scintillators and semiconductors are described in §3.2 and §3.3.

3.1 Information carrier statistics

This issue of information carrier statistics was addressed by Fano[3] in the context of gas detectors. Fano proposed that in the case where all the energy of the incident radiation is deposited in the detector, the variance in the number of information carriers generated should be proportional to the variance given by Poisson statistics. Suppose we have an incident particle of energy E_0, and energy $w = E_0 / \overline{n}$ is required on average to produce an information carrier if on average $\overline{n}$ information carriers are generated in the deposition of E_0. According to Poisson statistics, which applies to many random counting problems, the variance in the number of information carriers will be equal to $\overline{n}$ [2]. The variance in our case is then

$$\sigma_n^2 = F\overline{n} = FE_0 / w \tag{3.1}$$

16

where the Fano factor is defined as[3]

$$F = \frac{\left\langle (n - \bar{n})^2 \right\rangle}{\bar{n}}.$$

(3.2)

It is useful to know how many showers, or primary particles, must be simulated in order to obtain an adequate estimate for F. The variance of the Fano factor can be calculated from the variance of sample variance s and the variance of the sample mean $\bar{n}$. For each of N showers simulated n_i information carriers are produced, and the sample variance and mean are defined as

$$s = \frac{1}{N-1} \sum_{i=1}^{N} (n_i - \bar{n})^2, \quad \bar{n} = \frac{1}{N} \sum_{i=1}^{N} n_i$$

(3.3)

and $F = s/\bar{n}$. The variances of these quantities are[20]

$$\sigma_s^2 = \frac{2s^2}{N}, \quad \sigma_{\bar{n}}^2 = \frac{s}{N}.$$

(3.4)

From the standard prescription for error propagation,

$$\begin{aligned}
\sigma_F^2 &= \left(\frac{\partial F}{\partial s} \right)^2 \sigma_s^2 + \left(\frac{\partial F}{\partial \bar{n}} \right)^2 \sigma_{\bar{n}}^2 \\
&= \left(\frac{1}{\bar{n}} \right)^2 \frac{2s^2}{N} + \left(-\frac{s}{\bar{n}^2} \right)^2 \frac{s}{N}. \\
&= \left(2 + \frac{F}{\bar{n}} \right) \frac{F^2}{N}
\end{aligned}$$

(3.5)

Since in most cases of interest $\bar{n} \gg 1$, one can use as the standard deviation in F

$$\sigma_F \approx F \sqrt{2/N}.$$

(3.6)

This means 20,000 showers are needed to know F with 1% precision.

F can be thought of as the ratio of the sample variance in information carriers or counts divided by what it would be if Poisson statistics held. It is

17

important to note that this component of energy resolution, expressed as a

fractional error, is proportional to

$$\sigma_n/n = \sqrt{F/n} = \sqrt{Fw/E_0} \tag{3.7}$$

rather than F, so w is just as important. On the experimental side, resolution is

expressed as the full width at half-maximum (FWHM) of a peak as a percentage

of its energy. Approximating the peak as Gaussian, the component due to pair

creation is

$$R \approx 100\% \times 2.355\, \sigma_n/n. \tag{3.8}$$

The Fano factor will always be in the range $0 - 1$, so we expect the energy

resolution better than or equal to that given by Poisson statistics.

That $F \leq 1$ can be understood intuitively as follows. Consider a random

counting process, where n could be the number of decays recorded from a

radioactive source or the flux of photons in a particular energy range coming from

a star over a given time interval. One could calculate that $\bar{n}$ counts on average

are expected over a certain time period, but in any interval there could be no

counts, and there is effectively no upper limit for n. Our situation is

fundamentally different. Suppose our detector uses an "ideal" material with

bandgap E_G, and that the entire energy of the gamma-ray is deposited in the

detector, and furthermore all of E_0 goes into the production of electron hole pairs.

No energy is lost to lattice oscillations (phonons) or otherwise. A gamma-ray of

energy E_0 could produce at most E_0/E_G pairs. More importantly though, the

energies of all N electron-hole pairs w_i resulting from a single gamma-ray are

constrained by energy-conservation as

$$E_0 = \sum_{i=1}^{N} w_i \qquad (3.9)$$

which would not be required in a random counting process. In some silicon or

germanium detectors, the above situation is nearly realized and $F \sim 0.1$ has been

observed[21-24] after one accounts for incomplete charge collection and noise

from the detector electronics (see §3.3). In all cases though, some of E_0 is lost,

that is, not partitioned into information carriers. The more prevalent these losses

are, the closer we will be to Poisson statistics in describing the overall energy

resolution.

Even when E_0 is in its entirety partitioned into the information carriers w_i

F takes a finite value because the energy of each w_i is random according to some

distribution. Suppose, for example, $E_0 = 100 \, \text{keV}$ and w_i can be as low as 1 eV

or as high as 20 eV. Equation (3.9) still applies, but F would be much higher than

it is in silicon or germanium since the partitioning of E_0 into electron-hole pairs

is now less deterministic. If w_i had approximately the same value for all

information carries, F would approach zero. Lastly, it is important to remember

that F and w are meant to describe intrinsic properties of materials. Taking

semiconductors (§3.3) as an example, incomplete charge collection and noise

from the diode electronics do not figure into F and w, but phonon losses would.

3.2   Energy resolution in scintillators

We begin with scintillators, since they provide a convenient context to discuss error propagation in multiplication processes.[2] Noise from a scintillation counter may be divided into three sources: conversion of the energy of the incoming radiation to electron-hole pairs in the scintillation material (see above), probability a given electron-hole pair will produce a photon that is registered in the photomultiplier tube (PMT), and multiplication by the dynodes. For simplicity, let us consider the case where the entire energy of the gamma-ray is deposited in the scintillator. The following calculation of energy resolution (based on Delaney and Finch 1992[2]) is a rough approximation, but is useful in illustrating the relative importance of the three sources of error stated above.

There is no general expression for the variance in the number of photons that strike the photocathode. To obtain this variance we would need to understand, for the particular scintillating material and geometry involved, the complicated process by which the energy of the incident particle is converted to electron-hole pairs and efficiency with which these relax yielding photons. We would also need to consider any losses due to photons that do not reach the photocathode.

To calculate the probability an electron-hole pair is recorded one must multiply three inefficiencies: the probability p_{scint} an electron-hole pair will produce a scintillation photon, the transfer probability p_{trans} the photon will reach the photocathode, and the quantum efficiency of the photocathode. The quantum efficiency of the photocathode can be defined as the probability p_{PC} that a

photoelectron will be released and is collected at the first dynode when a photon strikes the photocathode. The number n of electron-hole pairs is taken as given at this stage, so there are n events that can each have one of two outcomes – either a photoelectron reaches the first dynode or it doesn't. This process is therefore described using the binomial distribution. The corresponding variance is derived as follows. From the definition of variance

$$\sigma^2 = \frac{1}{n} \sum_{i=1}^{n} (x_i - p)^2,$$
$$p = p_{scint} \times p_{trans} \times p_{PC}$$

(3.10)

where $x_i = 1$ if an electron-hole pair results in a photoelectron at the first dynode and $x_i = 0$ if it does not. One expects pn terms for the former case and $(1-p)n$ for the latter. The variance in the average number of photoelectrons produced for a single electron-hole pair is then

$$\sigma^2 = p(1-p)^2 + (1-p)p^2$$
$$= p(1-p)$$

(3.11)

or, for all n, $\sigma^2 = np(1-p)$.[2]

For the treatment of error due to multiplication in the photomultiplier tube, following Delaney and Finch[2], we consider a process beginning with a single electron striking the first dynode where it is multiplied with a gain m_1. The resulting electrons then encounter the second dynode where they are multiplied by m_2 and so on, until the pulse has been multiplied with gain m_n by the final dynode. For each dynode gain m_i there will be a variance σ_i^2 in the

21

multiplication for each individual electron that strikes dynode i. The total variance for a pulse due to a single initial electron is

$$\sigma^2 = \sigma_1^2 \prod_{i=2}^{n} m_i^2 + m_1 \sigma_2^2 \prod_{i=3}^{n} m_i^2 + m_1 m_2 \sigma_3^2 \prod_{i=4}^{n} m_i^2 + \ldots + \prod_{i=1}^{n-1} m_i \sigma_n^2 . \qquad (3.12)$$

Equation (3.12) may be interpreted as follows: The variance due each dynode is enhanced by multiplication from subsequent dynodes, so the total number of electrons produced on average by a single electron incident on dynode i ($m_i m_{i+1} \ldots m_n$) will have variance $\sigma_i^2 m_{i+1}^2 \ldots m_n^2$. Since the cascade resulting from each electron incident on dynode i can be taken as independent, term i will be multiplied by the expected number of electrons incident on that dynode – 1, m_1, and $m_1 m_2$ for the first three dynodes.

It will be more convenient to write (3.12) in terms of the relative variance $\mathcal{V}$ which is defined as the variance divided by the signal squared. For the total variance, the signal refers to the total number of electrons ejected from the final dynode. For the individual dynodes it is respective gain m_i of dynode i (so $\mathcal{V}_i = \sigma_i^2 / m_i^2$). Dividing (3.12) by $\prod_{i=1}^{n} m_i^2$,

$$\mathcal{V} = \mathcal{V}_1 + \frac{\mathcal{V}_2}{m_1} + \frac{\mathcal{V}_3}{m_1 m_2} + \ldots + \frac{\mathcal{V}_n}{\prod_{i=1}^{n} m_i} . \qquad (3.13)$$

This general result for error propagation in multiplication processes will be used again shortly.

Consider the case where all dynodes have identical gain m_0 except for the first one, which is often given a greater gain in order to improve energy resolution. (3.13) becomes

$$\mathcal{V} = \mathcal{V}_1 + \frac{\mathcal{V}_0}{m_1}\left(1 + \frac{1}{m_0} + \frac{1}{m_0^2} + \ldots + \frac{1}{m_0^{n-2}}\right).$$

Noting that the terms in parentheses form a geometric series, we have

$$\mathcal{V} \approx \mathcal{V}_1 + \frac{\mathcal{V}_0}{m_1}\frac{m_0}{m_0 - 1}. \tag{3.14}$$

The variance in dynode gain is approximated as Poisson noise, giving $\mathcal{V}_i = 1/m_i$ and

$$\mathcal{V}_{dynode} \approx \frac{m_0}{m_1(m_0 - 1)}. \tag{3.15}$$

To obtain the energy resolution for the entire scintillator, including the photomultiplier tube, we again use the result for error propagation in multiplication processes given by (3.13). Rather than having a term for each subsequent dynode, there will only be three terms. The first will represent variation in the number of electron-hole pairs due to a single radiation particle interacting with the scintillator material. The second accounts for the efficiency of converting electron-hole pairs to photoelectrons, and the third the whole series of dynodes. The relative variances are

$$\mathcal{V}_{e-h} = \frac{Fn}{n^2} = \frac{F}{n},$$

$$\mathcal{V}_{PE} = \frac{p(1-p)}{p^2} = \frac{1-p}{p},$$

23

and (3.15). The relative variance for the scintillation counter is then

$$V_{scint} = V_{e-h} + \frac{V_{PE}}{n} + \frac{V_{dynode}}{np}$$

$$= \frac{1}{n}\left(F + \frac{1-p}{p} + \frac{m_0}{m_1(m_0-1)p}\right).$$

(3.16)

Taking the square root of (3.16) we have σ_N/N where N is the total number of counts in a pulse. σ_N/N is essentially equivalent to the energy resolution. If this is expressed in terms of the full width at half maximum (FWHM), then, approximating a Gaussian peak, $\Delta E_{FWHM}/E \approx 2.355\, \sigma_N/N$. Expressing this width in terms of the gamma-ray energy and average electron hole pair energy (see §3.1)

$$\frac{\Delta E_{FWHM}}{E} = 2.355\left[\frac{w}{E}\left(F + \frac{1-p}{p} + \frac{m_0}{m_1(m_0-1)p}\right)\right]^{1/2}.$$

(3.17)

Assuming typical values of $F \sim 0.1$, $p \sim 0.1$, $m_1 = 6$, and $m_0 = 4$,

$$\frac{\Delta E_{FWHM}}{E} = 2.355\left[\frac{w}{E}\left(0.1 + 9 + \frac{8}{9}\right)\right]^{1/2}.$$

(3.18)

The photocathode is the limiting factor in energy resolution as quantum efficiencies for photocathodes are currently $< 30\%$.[2]

It is clear from (3.18) that, aside from w, the statistics involved in electron-hole pair production are currently of little consequence in scintillators. As the quality of scintillator crystals improves, and if photodetectors with vastly superior quantum efficiency become available, this may no longer be the case.

3.3   Energy resolution in semiconductors

Semiconductor detectors generally have much better energy resolution than scintillators. As seen in §3.2 the photomultiplier tube causes much of the peak broadening in scintillators, and semiconductors do not rely on any photodetector. Also the average electron-hole pair energy w is much lower in semiconductors due to their narrower bandgaps which improves resolution by increasing the number of information carriers, as in (3.7). Silicon and germanium, for example, have bandgaps of roughly 1.1 and 0.7 eV (and $w = 2.96, 3.62$ eV [25]), whereas NaI has a bandgap of ~6 eV[10].

Despite the absence of a photodetector, energy resolution in semiconductors does not currently approach that suggested by the Fano factor alone. The transport of electrons and holes across the detector material is imperfect, so there will be a contribution ΔE_{ICC} from inefficient charge collection. Noise (ΔE_{Elec}) is also introduced by the electronics, which includes an amplifier [10]. Both the Fano and charge collection components will increase with the energy of the incident radiation, whereas the component from the electronics can be taken as constant[2, 26]. If charge collection is treated in terms of quantum efficiency, as in §3.2, then for semiconductors

$$\frac{\Delta E_{FWHM}}{E} = 2.355 \left[wF/E + \Delta E_{ICC}^2 / E^2 + \Delta E_{Elec}^2 / E^2 \right]^{1/2}$$

$$= 2.355 \left[\frac{w}{E} \left(F + \frac{1-p}{p} \right) + \Delta E_{Elec}^2 / E^2 \right]^{1/2} \tag{3.19}$$

if p is the probability that an information carrier is not trapped in the

semiconductor.

4   Electron Cascade Simulation

To calculate the number of electron hole pairs, a reliable model for electron inelastic scattering is needed. This chapter is concerned with inelastic electron scattering and the resulting cascade process, which is the main focus of this work. In the following sections, where models for these processes are developed, both the quantities cross section (σ) and inverse mean-free-path (IMFP, μ) are used. These are related as

$$\mu = \sigma \frac{\rho N_A}{M} \tag{4.1}$$

where $N_A \approx 6.022 \times 10^{23}$ is Avogadro's number and M is the molar mass of the constituent atom or compound.

Observed EELS spectra reveal that the dominant inelastic scattering processes for fast electrons are plasmon excitation, single valence electron excitation, and the ionization of the most loosely bound atomic subshells. In the final stages, for low energy electrons and holes, excitation of optic phonons can be significant and here we adopt a model based on measured infrared refractive index and absorption coefficient. A combination of valence electron excitations across the bandgap, plasmon excitations, inner shell excitations, and optic phonon scattering is sufficient to provide a complete description of inelastic electron scattering. We separate the measured spectra into the first three components by fitting functions based on theoretical modeling and we also use theory to describe the relative variation of all four components with electron energy. EELS data for silicon[27] is shown in Figure 7.
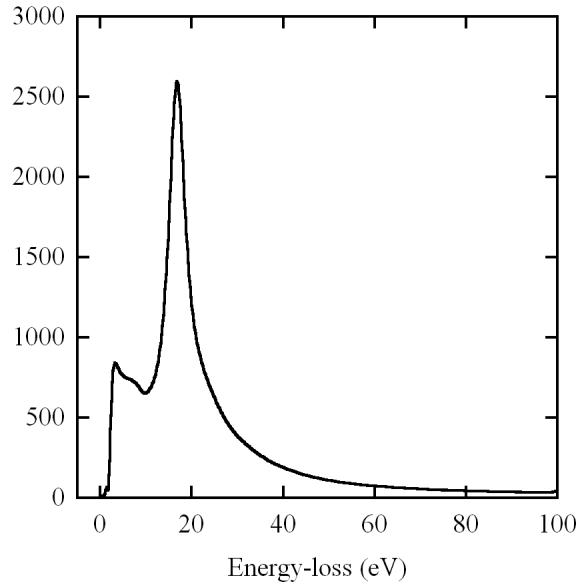
Figure 7. Electron energy-loss spectrum for silicon. The peaks at ~3 and 16.7 eV are due to valence electron and plasmon excitation respectively.

Some background information on energy bands in solids and sampling algorithms is given in §4.1 and §4.2. The physical models used for inelastic electron scattering are described in §4.3 — §4.6. In §4.9 output from our code is discussed, both for a generic model and for silicon.

4.1   Energy bands in solids

The end result of each shower is a distribution of electrons in the conduction band and holes (vacant electronic states) in the valence band. Since the nature of these energy bands is central to this study, a brief review of the topic is in order. For isolated atoms, as in a monatomic gas, there exist discrete energy levels. In molecules the atoms, and hence electrons in identical quantum states, are in close proximity. According to the Pauli exclusion principle two fermions cannot share the same state[28]. Electronic energy levels therefore split into several closely spaced states. The most energetic occupied state at low temperature is called the

28

HOMO (highest occupied molecular orbital) level, and the lowest unoccupied state the LUMO level. In a solid quantum states split in energy to such an extent that the closely spaced states can be treated as a continuum. The states analogous to those below the HOMO level form the valence band and the higher states form the conduction band. In a semiconductor or insulator these states are separated by the bandgap. A generic illustration of these energy states is given in Figure 8.
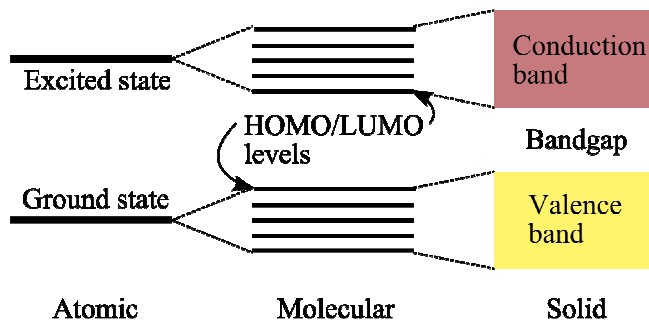
Figure 8. Generic electronic energy levels for an atom, molecule, and solid semiconductor or insulator.

Obviously, the situation is more complicated in reality. For most elements only the most loosely bound electrons, the valence electrons, form the valence band. It is these electrons that are responsible for chemical bonding. For the purposes of this study valence electrons are considered distinct from the inner shell electrons in a solid, which are more tightly bound and can be thought of as occupying discrete energy states as in isolated atoms (though the binding energies are to some extent shifted from their atomic values[29]). It can be seen from calculated densities of states that the more loosely bound inner shell electronic states (~ 20 eV from the bandgap) are slightly dispersed in energy. In modeling plasmon and single electron excitation, it is important to maintain a consistent distinction between the valence band and inner shell (or atomic) states.

4.2   Sampling inelastic processes

Each scattering event is sampled in the following way: A random number in the

range $0-1$ is drawn from a uniform distribution to decide whether a valence

electron excitation, plasmon excitation, inner shell excitation, or phonon

scattering takes place. For an electron with kinetic energy E_i, the probability

$P(j \mid E_i)$ for process j is equal to energy-dependent inverse mean-free-path

$\mu_j(E)$ (or cross section) divided by the sum of inverse mean-free-paths for all

processes. This is expressed as

$$P(j \mid E_i) = \frac{\mu_j(E_i)}{\sum_j \mu_j(E_i)}. \tag{4.2}$$

If escape from the detector is not considered, one is concerned with the relative

mean-free-paths of different processes, not absolute distances or cross-sections.

A probability density function (PDF) $p_j(\Delta E \mid E_i)$ can be defined for each

process, where an energy loss ΔE is suffered by an electron of initial energy E_i:

$$p_j(\Delta E \mid E_i) = \frac{d\mu_j(E_i)}{d\Delta E} \bigg/ \mu_j(E_i). \tag{4.3}$$

For a normalized PDF

$$\int_0^{E_i} p_j(\Delta E \mid E_i) \, d\Delta E = 1. \tag{4.4}$$

As with the differential IMFP or angle-integrated differential cross

section, the PDF is proportional to the probability that an amount of energy in the

differential interval $d\Delta E$ about ΔE will be lost. For the chosen process (phonon

scattering excluded), the energy-loss is determined by drawing another uniform

30

random number which is used to sample the cumulative PDF for that process, as

in (4.5) where R is a random number from $0 - 1$ and the PDF is normalized.

$$R = \int_0^{\Delta E} p(\Delta E' \mid E_i) d\Delta E' \tag{4.5}$$

This prescription for sampling the DCS is illustrated in Figure 9 (which represents

no particular material), where the vertical arrows point to the energy lost by the

incident electron in plasmon or valence excitation.
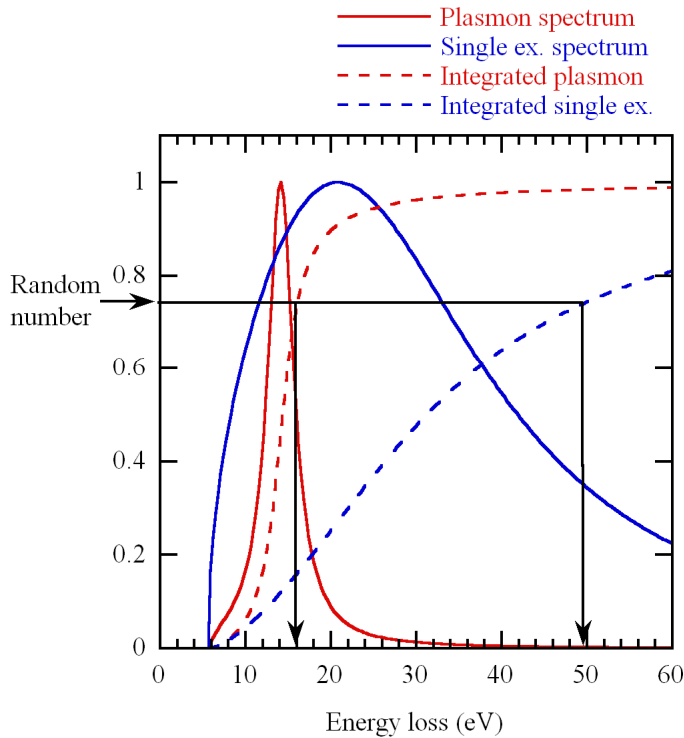
Figure 9. Energy-loss spectrum and integrated energy-loss spectrum for plasma decay and valence excitation. All are scaled so their maxima are 1.

Depending on the form of $p_j(\Delta E \mid E_i)$ one could solve for ΔE in (4.5)

analytically, or even use a root finding routine to quickly reach the answer

numerically. To keep things simple, and to allow for any PDF, the PDF is stored

as an array for a logarithmic grid of ΔE values, unless it is stated otherwise. For

plasmon and valence excitation, this grid spans from the bandgap width E_G to

whatever energy is required for the initial fast electron. Losses from inner shell

ionization are sampled by using the grid of secondary electron energies E_s

provided in the LLNL database[30], which is related to the energy loss as

$\Delta E = E_B + E_s$ where E_B is the binding energy of the subshell in question.

The procedure for sampling the energy loss PDF for these three processes

is as follows. Suppose the PDF of a variable x is a function $p(x)$ whose values

p_i are known for points x_i. A cumulative PDF $s(x)$ is defined at points x_i as

$$s_i = \int_{x_1}^{x_i} p(x)dx = \sum_{i=2}^{i} \tfrac{1}{2}(p_{i-1} + p_i)(x_i - x_{i-1}), \quad (s_1, s_{max}) = (0,1) \qquad (4.6)$$

and the derivative of $p(x)$ is

$$p_i' \equiv \frac{dp}{dx}_i = \frac{p_{i+1} - p_i}{x_{i+1} - x_i}. \qquad (4.7)$$

To generalize (4.5),

$$R = \int_{x_1}^{x} p(x')dx'. \qquad (4.8)$$

In equations (4.6) — (4.8), it is assumed that s, p, and p' have been normalized by

dividing by

$$s_{max} = \int_{x_1}^{x_{max}} p(x)\,dx = \sum_{i=2}^{i_{max}} \tfrac{1}{2}(p_{i-1} + p_i)(x_i - x_{i-1}). \qquad (4.9)$$

Random number R is compared to values s_i. After it is determined that

$s_i < R < s_{i+1}$, x is found by interpolating according to (4.6) and (4.7). This

calculation is illustrated in Figure 10, where R is equal to the sum of the areas of

regions $1 - 3$, which are equal to the first, second and third terms in
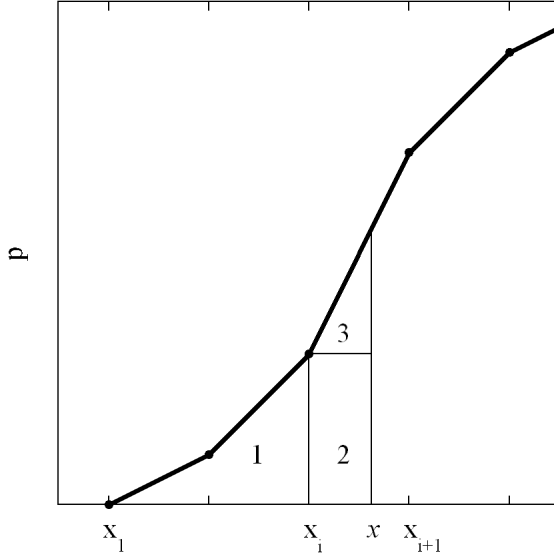
Figure 10. Illustration of the algorithm used for sampling a discrete probability density function (PDF).

$$R = s_i + p_i(x - x_i) + \tfrac{1}{2} p_i'(x - x_i)^2 .\tag{4.10}$$

Using the quadratic equation,

$$x = x_i + \frac{p_i}{p_i'}\left[\sqrt{1 + 2(R - s_i)\, p_i'/p_i^2} - 1\right].\tag{4.11}$$

If $2(R - s_i)\, p_i'/p_i^2 \ll 1$ (4.11) will fail. Approximating the square-root

accordingly,

$$\begin{aligned}
x &= x_i + \frac{p_i}{p_i'}\left[1 + (R - s_i)\, p_i'/p_i^2 - 1\right]\\
&= x_i + \frac{R - s_i}{p_i}
\end{aligned}\tag{4.12}$$

which is the result one obtains neglecting region 3.

4.3 Plasmon excitation

Plasmon excitation is generally the dominant feature in EELS spectra, and it is crucial that it is treated accurately. Plasmons are collective oscillations of valence electrons which decay by exciting a valence electron into the conduction band[31, 32]. The plasmon resonance occurs at energy-loss ΔE where the inverse of the real part of the dielectric function $\varepsilon(q, \Delta E)$, where $\mathbf{q}$ is the scattering vector, passes through zero[31, 32]. This corresponds to the peak at 16.7 eV in Figure 7.

In our code plasmon excitation is modeled using the following inverse mean-free-path for a free electron gas given by Ritchie and Howie[33] (in CGS units),

$$\frac{d\mu}{d\Delta E} = \frac{2e^2}{\pi\hbar^2 v^2} \int_{q_{min}}^{q_c} \frac{dq}{q} \operatorname{Im}\left(-\frac{1}{\varepsilon(q, \Delta E)}\right). \tag{4.13}$$

v represents the velocity of the incident electron, and the energy-loss function is

$$\operatorname{Im}\left(-\frac{1}{\varepsilon(q, \Delta E)}\right) = \frac{\Delta E \hbar \Gamma E_P^2}{\left(\Delta E^2 - E_q^2\right)^2 + \Delta E^2 \hbar^2 \Gamma^2}$$

where E_P is the non-dispersed plasmon energy and Γ is the damping constant. In this model plasmon dispersion is given by

$$E_q^2 = E_P^2 + \tfrac{3}{5}\alpha\left(\hbar v_F q\right)^2 \tag{4.14}$$

where α is a constant of order unity and v_F is the Fermi velocity in the detector material. The constant α is estimated by fitting this model (along with valence excitation) to an EELS spectrum. In the case of silicon we find $\alpha \sim 2$. The lower limit of integration in (4.13) is

34

$$q_{min} = \frac{\sqrt{2}m}{\hbar}\left[v^2 - E_q/m - v\left(v^2 - 2E_q/m\right)^{1/2}\right]^{1/2},$$

the lowest dynamically allowed scattering wave-vector[33], where m and v are the relativistic mass and velocity of the incident electron. The upper limit is critical scattering vector q_c, above which only valence electron excitations occur[31]. Invoking energy and momentum conservation, q_c is found by solving

$$E_q = \frac{\hbar^2}{2m}\left(q_c^2 + 2q_c q_F\right)$$

where q_F is the Fermi scattering vector. Since E_q is a function of q_{min} and q_c respectively in the above two equations, there are no simple analytic solutions and numerical methods are therefore used. The integral in equation (4.13) is evaluated using trapezoidal integration.[34] Since the scattering process is chosen before the energy-loss, the integrated inverse mean-free-path is required. This is calculated by integrating (4.13) over ΔE from the lowest possible loss (the band gap) to the energy of the incident electron. Plasmon excitation is not possible when the incident electron energy is so low that $q_{min} \geq q_c$. This situation occurs at a few times E_P for silicon. Differential energy-loss cross-sections for different incident electron energies are plotted in Figure 11. At higher electron energies plasmon dispersion becomes less important and the differential cross section (DCS) resembles a Lorentzian distribution centered on E_P.
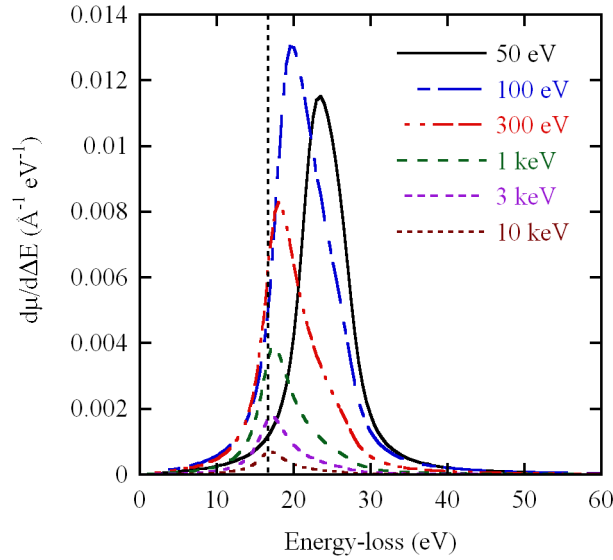
Figure 11. Differential energy-loss inverse mean-free-path in silicon (proportional to DCS) for plasmon excitation with different incident electron energies. The vertical dotted line indicates the plasmon energy without dispersion, which is about 16.7 eV for silicon.

Finally, the model simulates plasmon decay by valence electron excitation. Fraser[7] and Gao et al.[8, 9] assumed that each plasmon would give rise to five electron-hole pairs. A more complete theory for plasmon decay was proposed by Chung and Everhart[35]. Similar to an electron of the same energy the plasmon can excite electrons from the valence band to the conduction band. The probabilities of various excitations are then given by similar expressions, as is described in §4.4.

4.4 Valence electron excitation

To calculate the differential cross section for valence electron excitations across the bandgap wave functions for valence and excited conduction electron states are needed. In principle these could come from density functional theory codes, but

there are still potential complications from many electron and excitonic effects
that can not be treated properly within a one electron theory.

For fast electrons we choose instead to take the measured differential cross
section from EELS and parameterize it by the following function of energy loss

$$\frac{d\sigma}{d\Delta E} \propto \left[A(\Delta U - 1)^{-1/2} + (B\Delta U + 1)^{5/2} \right]^{-1} \tag{4.15}$$

where $\Delta U = \Delta E / E_G$, the energy lost by the incident electron divided by the
bandgap. This function is chosen for its simplicity and because it generally
provides a good match to the valence excitation component of an EELS spectrum.
Parameters A and B are related to the peak of this distribution by

$$A = 5B(\Delta U_{peak} - 1)^{3/2} (B\Delta U_{peak} + 1)^{3/2} .$$

Values $\Delta U_{peak} = 2.5$ and $B = 0.03$ are obtained fitting (4.15) along with the above
plasmon model (§4.3) to the silicon EELS spectrum in Figure 7.

The energy of the resulting secondary electron(s) is then calculated as
illustrated in Figure 12. For each event, a valence electron with random energy
E_b is excited into the conduction band. The energy lost by the incident electron
is partitioned between the secondary and a hole left in the valence band. An
incident electron with energy E_i will then have its energy reduced to

37
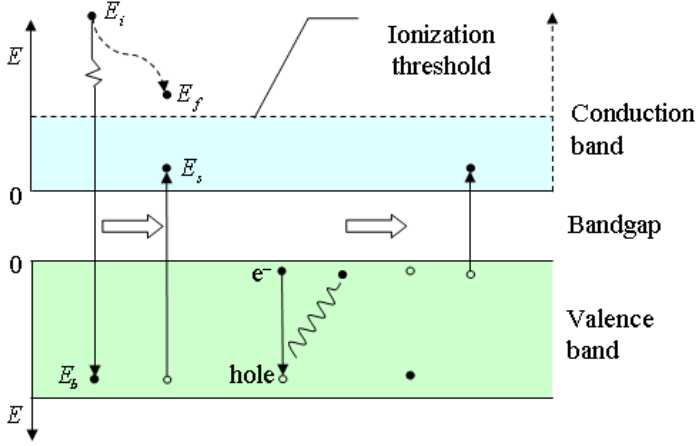
Figure 12. Generation of a secondary electrons by valence band ionization (left) and by relaxation within the valence band (right).

$$E_f = E_i - \Delta E = E_i - (E_s + E_b + E_G) \tag{4.16}$$

where E_s is the energy of the secondary electron and E_G the bandgap. Additional valence electrons can be excited to the conduction band when valence electrons relax to holes left by the process described above, transferring the difference in energy to another valence electron. This relaxation process is only possible if the valence band is broader than the bandgap, or if an inner shell is ionized (not shown). The model used for relaxation is discussed in greater detail in §4.7.

In the following calculations the valence band density of states (DOS) $\rho_V(E_b)$ either takes an arbitrary form, which is given for an array of energies in an input file, or is assumed to be uniform, with only the width E_V specified. The conduction band is approximated as having a free-electron density of states.

After ΔE has been calculated it remains to determine the energies of the ionized valence electron and E_s. This is accomplished by sampling the valence electron energy E_b from a PDF

$$p(E_b \mid \Delta E) \propto \rho_V(E_b)\rho_C(E_s), \quad E_s = \Delta E - E_b - E_G \qquad (4.17)$$

which is related to the joint density of states for the excitation of a valence

electron to the conduction band. Approximating the conduction band as having a

free electron density of states ($\propto E^{1/2}$)

$$p(E_b \mid \Delta E) \propto \rho_V(E_b)(\Delta E - E_b - E_G)^{1/2} . \qquad (4.18)$$

This PDF is sampled as described in §4.2.

In the case where a uniform density of states is assumed for the valence

band, this sampling may be performed analytically. $\rho_V \to 1$ and (4.18) becomes

$$p(E_b \mid \Delta E) \propto (\Delta E - E_G - E_b)^{1/2} . \qquad (4.19)$$

The analogue of (4.8) is

$$R = \frac{\int_0^{E_b} (\Delta E - E_G - E_b')^{1/2} dE_b'}{\int_0^{E_b^{\max}} (\Delta E - E_G - E_b')^{1/2} dE_b'}, \quad E_b^{\max} = \min(E_V, \Delta E - E_G) \qquad (4.20)$$

where E_V is the width of range of energies spanned by the valence band, and the

upper limit of integration in the denominator is understood in terms of energy

conservation. Evaluating these integrals and solving for E_b, one obtains

$$E_b = (\Delta E - E_G)\left(1 - \left\{1 - R\left[1 - \left(1 - \frac{E_b^{\max}}{\Delta E - E_G}\right)^{3/2}\right]\right\}^{2/3}\right). \qquad (4.21)$$

When $\Delta E - E_G < E_V$ this simplifies to

$$E_b = (\Delta E - E_G)\left[1 - (1-R)^{2/3}\right], \quad 1 - R \Rightarrow R$$
$$= (\Delta E - E_G)(1 - R^{2/3}). \qquad (4.22)$$

If $\Delta E - E_G \gg E_V$ the density of states of free electrons is no longer relevant in the present context and E_b may then be chosen from anywhere in the valence band with equal probability. Therefore, after ΔE has been found in the case of a uniform valence band DOS,

$$E_b = \begin{cases} (\Delta E - E_G)(1 - R^{2/3}) , & \Delta E - E_G \leq E_V \\ (\Delta E - E_G)\left(1 - \left\{1 - R\left[1 - (1 - E_V/(\Delta E - E_G))^{3/2}\right]\right\}^{2/3}\right), & \Delta E - E_G > E_V \\ RE_V , & \Delta E - E_G \gg E_V \end{cases}$$

(4.23)

Whether or not a uniform valence DOS is assumed, $E_s = \Delta E - E_G - E_b$ is given from energy conservation.

For energies below 20–30 eV the energies of the scattered and ejected electron are not very different, and exchange effects become important[36]. The above approach based on EELS will then no longer be adequate. Ideally a model based on wave functions taken from density functional electronic structure codes (such as VASP[37, 38]) would be used. This is both time consuming and, in practice, limited to a narrow range of energies in the conduction band. Instead, following Ziaja, London, and Hajdu[39], the random k approximation is used to simulate single electron transitions across the bandgap, considering only the densities of states ρ of the valence and conduction bands. The binding energy E_b of the ionized valence electron is determined first. Integrating over all possible final states of the incident and ionized electrons, the conditional

probability of an electron of energy E_i ionizing a valence electron of initial

energy E_b is proportional to

$$p(E_b \mid E_i) \propto \rho_V(E_b) \int \rho_C(E_s) \rho_C(E_f) dE_s$$

where secondary energy E_s is the energy of the valence electron after it is ionized

and E_f is the final energy of the incident electron as defined in (4.16).

Since electrons are interchangeable, we define $E_f \geq E_s$. This gives an

upper limit $E_s^{\max} = \frac{1}{2}(E_i - E_b - E_G)$. Again approximating the conduction band

with a free electron density of states ($\propto E^{1/2}$) the probability of a given valence

band excitation is

$$p(E_b \mid E_i) \propto \rho_V(E_b) \int_0^{E_s^{\max}} E_s^{1/2} \left[(E_i - E_b - E_G) - E_s \right]^{1/2} dE_s .$$

Defining the variable x as

$$x \equiv E_s / (E_i - E_b - E_G) \tag{4.24}$$

the probability for an excitation of a valence electron of energy E_b is now

$$p(E_b \mid E_i) \propto \rho_V(E_b)(E_i - E_b - E_G)^2 \int_0^{1/2} \sqrt{x(1-x)} \, dx \tag{4.25}$$

where the integral over x is just a constant. The probability density function

(PDF) for E_b is now

$$p(E_b \mid E_i) = \frac{\rho_V(E_b)(E_i - E_b - E_G)^2}{\int_0^{E_b^{\max}} \rho_V(E_b)(E_i - E_b - E_G)^2 \, dE_b} , \quad E_b^{\max} = \min(E_i - E_G, E_V) \tag{4.26}$$

where E_V is the difference in energy between the top and bottom of the valence

band.

The sampling is now over the valence band DOS modified by the squared term. When the initial electron energy is much greater than the sum of the valence band width and the bandgap

$$\left(E_i - E_b - E_G\right)^2 \approx E_i^2$$

and the sampling is effectively over the valence band DOS. During the execution of the code, $p(E_b \mid E_i)$ is stored as a 2-dimensional array, and is sampled as described in §4.2.

If the valence band DOS is taken as uniform, the above sampling is performed analytically. The PDF is that from (4.26) with $\rho_V \to 1$. Applying (4.8), E_b must be solved for in

$$R = \frac{\int_0^{E_b} (E_i - E_G - E_b')^2 \, dE_b'}{\int_0^{E_b^{max}} (E_i - E_G - E_b')^2 \, dE_b'}, \quad E_b^{max} = \min(E_i - E_G, E_V). \qquad (4.27)$$

This looks like (4.20), and the solution takes the same form:

$$E_b = (E_i - E_G)\left(1 - \left\{1 - R\left[1 - \left(1 - \frac{E_b^{max}}{E_i - E_G}\right)^3\right]\right\}^{1/3}\right). \qquad (4.28)$$

When $E_i - E_G \le E_V$ this simplifies as before. If $E_i - E_G > E_V$, the cubed term is expanded and the term in brackets multiplying random number R is

$$
\begin{aligned}
J &\equiv 1 - \left(1 - \frac{E_V}{E_i - E_G}\right)^3 \\
&= 3\left(\frac{E_V}{E_i - E_G}\right) - 3\left(\frac{E_V}{E_i - E_G}\right)^2 + \left(\frac{E_V}{E_i - E_G}\right)^3.
\end{aligned}
\qquad (4.29)
$$

Therefore, for $E_i < 30 \text{ eV}$ and a uniform valence DOS

$$E_b = (E_i - E_G) \begin{cases} (1 - R^{1/3}), & E_i - E_G \le E_V \\ \left(1 - \{1 - RJ\}^{1/3}\right), & E_i - E_G > E_V \end{cases}. \tag{4.30}$$

After E_b has been calculated, E_s is sampled from

$$\begin{aligned} p(E_s \mid E_i, E_b) &\propto \rho_C(E_s)\rho_C(E_i - E_s - E_b - E_G) \\ &\propto E_s^{1/2}(E_i - E_s - E_b - E_G)^{1/2} \end{aligned}. \tag{4.31}$$

Since it will be necessary to sample this distribution many times during the

execution of the code, it is worthwhile to seek an analytical method. The equation

that must be solved is

$$R = \frac{\int_0^{E_s} E_s'^{1/2}\left[(E_i - E_b - E_G) - E_s'\right]^{1/2} dE_s'}{\int_0^{E_s^{\max}} E_s'^{1/2}\left[(E_i - E_b - E_G) - E_s'\right]^{1/2} dE_s'} \tag{4.32}$$

where R is a random number in the interval $0-1$. If one defines

$$x \equiv \frac{E_s}{E_s^{\max}} = \frac{E_s}{\frac{1}{2}(E_i - E_b - E_G)} \tag{4.33}$$

(which differs from (4.24) by the factor of $\frac{1}{2}$) then (4.32) is, in dimensionless

form,

$$R = \frac{\int_0^x x'^{1/2}(2 - x')^{1/2} dx'}{\int_0^1 x'^{1/2}(2 - x')^{1/2} dx'}. \tag{4.34}$$

The integrals are simplified by approximating the integrand as follows:

$$\begin{aligned} x^{1/2}(2 - x)^{1/2} &= 2^{1/2} x^{1/2}(1 - \tfrac{1}{2}x)^{1/2} \\ &\approx 2^{1/2} x^{1/2}(1 - \tfrac{1}{4}x) \\ &= 2^{1/2}(x^{1/2} - \tfrac{1}{4}x^{3/2}). \end{aligned} \tag{4.35}$$

Ignoring normalization for the time being, the numerator in (4.34) is evaluated as

43

$$R \propto \tfrac{2}{3} x^{3/2} - \tfrac{1}{10} x^{5/2} \,. \tag{4.36}$$

Now another approximation is made. If one changes $x^{5/2} \to x^3$ (4.36) can be

evaluated using the quadratic formula if another variable is defined for $x^{3/2}$.

Replacing the fractions with constants a and b yields a quadratic equation

$$0 = bx^3 - ax^{3/2} + R \,. \tag{4.37}$$

Applying the constraint that $x = 1$ for $R = 1$, one obtains $b = a - 1$. a is found by

fitting the function

$$f(x) = ax^{3/2} - (a-1)x^3 \,. \tag{4.38}$$

to (4.34). This was done numerically with Matlab[R][40], with the result

$a \approx 1.160531$. (4.38) is plotted with in Figure 13. The derivative of (4.38) is also

plotted, along with the normalized integrand from (4.34). This amounts to a

comparison of the PDFs in addition to the cumulative PDFs (see §4.2) though

only the latter are used in the simulation. As seen in Figure 13, the approximation

introduces no appreciable error. Finally, applying the quadratic formula to (4.37)

$$x^{3/2} = \frac{a - \sqrt{a^2 - 4(a-1)R}}{2(a-1)} \tag{4.39}$$

and given (4.33)

$$E_s = \frac{1}{2}(E_i - E_b - E_G)\left[\frac{a - \sqrt{a^2 - 4(a-1)R}}{2(a-1)}\right]^{2/3} \,. \tag{4.40}$$
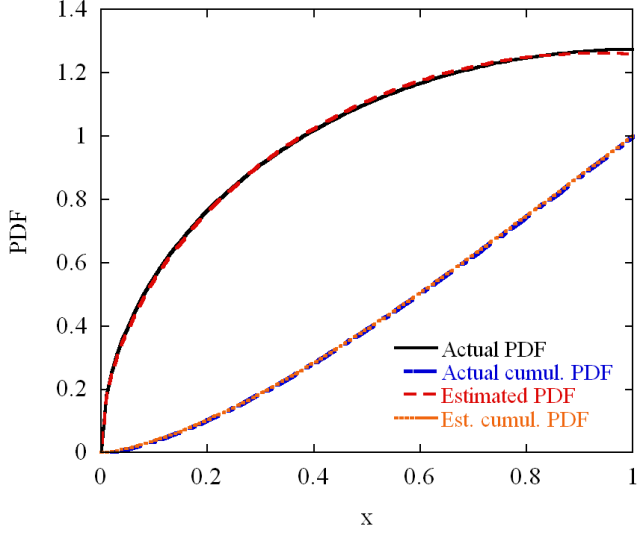
Figure 13. Estimation for sampling the low-energy, secondary electron PDF for valence electron excitation.

Since the probability of valence electron excitations compared to other electron scattering processes is needed to model scattering of electrons whose energies range from hundreds of keV to a few electron volts, the primary electron energy dependence of the cross section given by (4.15) is required. The energy-dependence for lower energies is based on the following analytic formula given by Bote et al[41], who used a Distorted Wave Born approximation to calculate the integrated cross section for inner shell ionization. If the overvoltage $U \equiv E_i/E_b$ is defined as the incident electron energy divided by the binding energy of the subshell in question, then for $U < 16$

$$\sigma_{Bote} = 4\pi a_0^2 \frac{U-1}{U^2}\left(a_1 + a_2U + \frac{a_3}{1+U} + \frac{a_4}{(1+U)^3} + \frac{a_5}{(1+U)^5}\right)^2. \qquad (4.41)$$

a_0 is the Bohr radius, and $a_1 - a_5$ are parameters specific to each element and electronic shell. The values of parameters a are found by extrapolating from values for subshells of similar character to the dominant contributions to the

45

valence band. For example this would be the 3p subshell for Si as the top of the valence band is mainly p-like. For all materials considered here, the valence band will be taken as p-type, and the same values for $a_1 - a_5$ will be used. For higher energies the dependence on the incident energy E_i is given by the Bethe-Powell formula[42] with the valence band binding energy E_b used in place of the binding energy E_{nl} of an orbital specified by quantum numbers n and l. Powell[42] calculates values for parameters c_{nl} for subshells of different elements, but for simplicity an intermediate value $c_{nl} = 0.8$ is used for the present simulations. If v is the velocity and m_0 the mass of the incident electron,

$$\sigma_{Bethe} \propto \frac{1}{v^2} \ln\left(\frac{c_{nl} m_0 v^2}{2E_{nl}} \right) \rightarrow \frac{1}{v^2} \ln\left(0.4 \frac{m_0 v^2}{E_{nl}} \right). \tag{4.42}$$

The velocity of the incident electron is related to its kinetic energy as[41]

$$\frac{v}{c} = \frac{\sqrt{E_i (E_i + 2m_0 c^2)}}{E_i + m_0 c^2}. \tag{4.43}$$

As discussed in §4.1 the valence band, unlike the inner shells, consists of many closely spaced states which can be treated as a continuum. The piecewise cross section given by (4.42) and (4.43) should therefore be convoluted with the valence band density-of-states $g(E_b)$. If the binding energy for valence electrons is defined within the range $E_G < E_b < E_G + E_V$, where E_V is the width of the valence band, then

$$\sigma_{SE}(E) = \int_{E_G}^{E_G + E_V} \begin{cases} \sigma_{Bote}(E, E_b), & U < 16 \\ \sigma_{Bethe}(E, E_b), & U \geq 16 \end{cases} g(E_b) dE_b. \tag{4.44}$$

There is still the issue that the angular momentum character of states changes from the bottom to the top of the valence band, although this is not addressed here.

4.5 Inner shell ionization

The inner shell excitations, included only when we model actual detector materials, are modeled by using the total and differential cross-sections from the Lawrence Livermore National Lab (LLNL) database[30]. Only inner shells with binding energies less than 100 eV or so are likely to make a significant contribution to the statistics of electron-hole pair creation. This means that M_{23} excitations in transition elements, N_{45} excitations in rare earths and O_{23} and O_{45} excitations in heavy elements. Converting the LLNL differential cross-sections to inverse mean-free-paths and comparing to the result for plasmons from §4.3, the prominence of plasmon excitation versus inner shell ionization is similar to that seen in EELS spectra. Vacancies created in atomic shells will relax to the valence band via radiative and Auger processes, which result in X-rays and electrons, respectively. The relaxation of vacancies is discussed in §4.7.

4.6 Optic phonons

For electron energies below the plasmon energy small losses due to optic phonons, in the 20-100 meV range, can significantly change the average electron-hole pair energy. Phonon scattering is fundamentally different from the other processes considered in this context because it results in energy losses to (or gains) that do not result in the creation of secondary particles. Since energy is

truly lost, rather than repartitioned among other particles, phonon scattering can significantly worsen energy resolution.

Drummond and Moll[43] give the average electron hole pair energy as

$$E_{e-h} = E_G + \left\langle E_K \right\rangle + \left\langle E_{ph} \right\rangle$$

where E_G is the band gap, $\left\langle E_K \right\rangle$ is the average energy of electrons and holes when they can no longer ionize and $\left\langle E_{ph} \right\rangle$ is the average energy loss due to optic phonons. The inverse mean-free-path is calculated using a prescription similar to that for plasmon excitation in §4.3. A single value $\Delta E = \hbar\omega_{opt}$ is used for the energy-loss (or gain in the case of phonon absorption), and optic phonons are approximated as non-dispersive. In analogy with (4.13)

$$\mu(E) = \frac{2e^2}{\pi\hbar v^2} I \int_{q_{min}}^{q_{max}} \frac{dq}{q} \tag{4.45}$$

$$I \equiv \int \text{Im}\left(-\frac{1}{\varepsilon(0,\omega)}\right) d\omega = \int \frac{2n(\omega)\kappa(\omega)}{\left(n(\omega)^2 + \kappa(\omega)^2\right)^2} d\omega, \tag{4.46}$$

where q_{min} and q_{max} are again the kinematic limits of the scattering vector. $n(\omega)$ and $k(\omega)$, the refractive index and attenuation, are obtained from optical data.[44] The integral (4.46) is evaluated by integrating the energy-loss function over the narrow range of frequencies corresponding to the optic phonon peak.

For the relevant conduction electrons, $E_i \approx \frac{1}{2}mv^2$ and $E_i \gg \hbar\omega_{opt}$. This allows for an analytic evaluation of the integral over q giving an inverse mean-free-path for phonon emission of

48

$$\mu(E_i) = \frac{m_e e^2}{\pi \hbar} I \frac{\ln\left(4 E_i / \hbar \omega_{opt}\right)}{E_i} .$$ (4.47)

The impact of phonon scattering depends on the ratio of the above inverse mean-free-path with that from the valence electron scattering model described in section 4.4. The ratio of phonon emission as opposed to absorption at temperature T is $\sim \exp\left(\hbar \omega_{opt} / k_B T\right)$, and (4.47) considers only phonon emission since it is based on the energy-loss function. At room temperature $k_B T \approx 0.026 \text{ eV}$, so if $\hbar \omega_{opt} \sim 0.05 \text{ eV}$ an electron is ~ 7 times more likely to loose energy due to phonon emission then to gain energy via absorption. Detectors which use narrow bandgap semiconductors such as germanium are cooled during operation. In many practical situations it is therefore expected that phonon emission will be much more probable than absorption.

The potential losses due to optic phonons in silicon, for example, have explicitly been simulationed by Fraser[7] and Gao et al[8] using a model given in [45]. This mean-free-path for electron scattering by optic phonons ultimately derives from measurements of hot electron emission from shallow p-n junctions by [46]. They give a value of 6 nm as the mean-free-path for scattering of 5 eV electrons by optic phonons, based on fitting simple transport equation solutions to their measurements of current transmitted across a junction. Their mean-free-path, given by

$$\lambda_{e-ph} = 4.52 \left(1 + \frac{E_i}{E_F}\right) \text{nm}^{-1}$$ (4.48)

implies an implausibly high electron scattering cross section by optic phonons.

Substantial scattering by optic phonons is only possible in materials with some degree of ionicity. This is evident from the theory given above where the cross section is proportional to the imaginary part of the inverse of the dielectric function that peaks at the frequency of the optic phonon. In silicon the 2 atoms in the primitive cell are identical in charge and not surprisingly the imaginary part of the dielectric constant or the attenuation part of the complex refractive index is small. Referring to Palik[44], $\kappa \sim 10^{-3}$ for Si but is of order unity for various compound semiconductors. Using (4.47) we estimate the mean-free-path for scattering of 5 eV electrons by optic phonon to be $2.0 \times 10^4 \, \text{nm}$. Energy-loss functions in the optic phonon energy-range are plotted in Figure 14 for silicon, germanium, zinc telluride, and gallium arsenide. These energy-loss functions were derived from optical data listed in Palik[44]. They illustrate the prominence of optic phonon scattering in compound semiconductors compared to silicon and germanium.
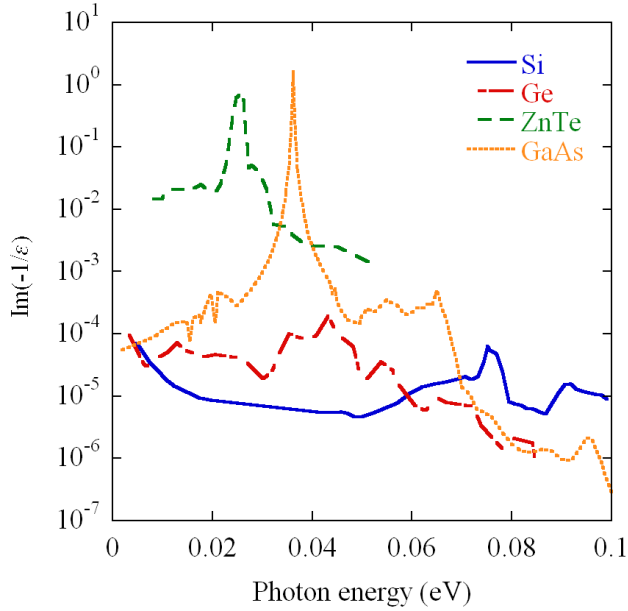
Figure 14. Optic phonon energy-loss functions from optical data for several semiconductors.

4.7 Relaxation

Vacancies in the atomic shells and in the valence band can produce secondary particles as they relax towards the top of the valence band. Relaxation of holes within the valence band can only result in an inter-band transition when the width of the valence band is greater than the bandgap $(E_V > E_G)$, as is the case for many semiconductors. For relaxation within the valence band and for transitions involving relaxation from an atomic state into the valence band, the energy of the relaxing valence electron is chosen according to the valence band DOS. Inter-band transitions that follow are treated as in §4.4 with ΔE given by the relaxation.

When simulating cascades that are initiated by a fast electron two types of relaxations are considered: Auger processes within the valence band, and the case where a valence electron fills an inner-shell vacancy and another valence electron

is ionized. After incorporating the inelastic electron scattering model into Penelope (§5), the relaxation model from that code is included, which consists of a comprehensive atomic model for radiative and non-radiative transitions[29].

4.8   Executing the Monte Carlo code

The above physical model, supported by EELS and optical data, provides material-specific input for the simulation. Input for this model is summarized in Table 1.

Table 1

Material-specific input.

Input	Symbol	Comments
Plasmon resonance energy	E_P	(eV) From EELS.
Plasmon decay constant	$\Delta E_P \equiv \hbar\Gamma$	(eV) From EELS.
Plasmon dispersion coefficient	α	(Unitless) From EELS.
Fermi energy	E_F	Used for plasmon dispersion.
Valence excitation peak	ΔU_{peak}	(eV) From EELS.
Valence excitation "tail" parameter	B	(Unitless) From EELS.
Plasmon to valence excitation ratio.	W_P	From EELS. Ratio of IMFPs at high-energy limit.
Inner shell data file	———	See §4.5
Optical phonon energy	$\hbar\omega_{opt}$	(eV) From optical data.
Integral of optical phonon energy-loss function	$\hbar I$	(eV) From optical data, see equation (4.46)
Effective bandgap	E_G	(eV)
Valence band DOS data file	———	Either DOS file or E_v is supplied
Valence band width	E_v	(eV) Required only if a uniform DOS is assumed.

Each shower is initiated with a fast electron of a given energy, and it is assumed that all particles stay within the detector material. The procedure for implementing the above model in a Monte Carlo scheme is as follows:

If the energy of an electron is less than a bandgap's width from the bottom of the conduction band, it cannot excite any other electrons and is added as one additional count for the current shower. Similarly, a hole, or vacant electronic state, in the valence band less than a bandgap's width from the top of the valence band also cannot result produce additional electrons via relaxation. If a secondary can excite other electrons, we return to it later. The primary electron moves on to the next interaction provided it is sufficiently energetic. All electrons generated in the current shower are followed until they cannot generate any more secondary electrons. After all showers are completed, the energy resolution is calculated from the tally of counts, or terminal electrons and holes, from each shower.

4.9 Results

The energy resolution due to the production of electron hole pairs is calculated for both a model system (§4.9.1) and silicon (§4.9.2). Energy resolution can depend on a detector material's bandgap, valence band, plasmon energy and width, and the relative probabilities of plasmon excitation, valence excitation, and inner-shell ionization. All the kinetic energy of the initial electron is assumed to be deposited, so the distribution of the number of electron-hole pairs per shower consists of a single peak, whose variance is used to define the energy resolution in terms of the Fano factor (3.2) and fractional FWHM (3.8).

4.9.1 Model system

In our model system a material is defined by five parameters: the bandgap E_G, valence band width E_V, plasmon energy E_P, plasmon width ΔE_P (or more precisely decay constant $\hbar\Gamma = \hbar/\tau$), and relative plasmon strength W_P, which is the ratio of integrated cross-sections for plasmons and valence excitation in the high-energy limit. It is expected that this ratio will remain constant for higher energies. For the model system, inner shells and phonons are not included, and a flat density-of-states is assumed for the valence band. The number of free parameters that determine the Fano factor is reduced to four by expressing the valence band width, plasmon energy, and plasmon width as multiples of the bandgap energy:

$$ F = f\left(\frac{E_V}{E_G}, \frac{E_P}{E_G}, \frac{\Delta E_P}{E_G}, W_P \right). $$

The incident electron energy is not considered a parameter because F is known not to depend on energy for electrons with energies in excess of ~1 keV. Plasmon dispersion, which in the model used here depends on the Fermi energy E_F and constant α (§4.3), is treated by taking $\alpha = 1$ and scaling E_F relative to silicon in the free-electron case which gives[19]

$$ E_F = E_F^{Si}(E_P/E_P^{Si})^{4/3}. $$

The parameters for the valence excitation model in §4.4 are also taken from the case of silicon.

We first fix the valence band width and investigate the variation of F with plasmon energy for relatively sharp plasmons, whose width is comparable to the band gap. As shown in Figure 15, where plasmons are 1, 4, 10, or 100 times more likely than valence electron excitations, the Fano factor oscillates as E_P is increased. Not surprisingly, these oscillations are damped down for broader plasmons and lower plasmon strength. For both values of ΔE_P, energy resolution depends little on plasmon energy when E_P is more than ~5 times the bandgap. For $E_P > 8 \, \text{eV}$, w varies by $< 6\%$.
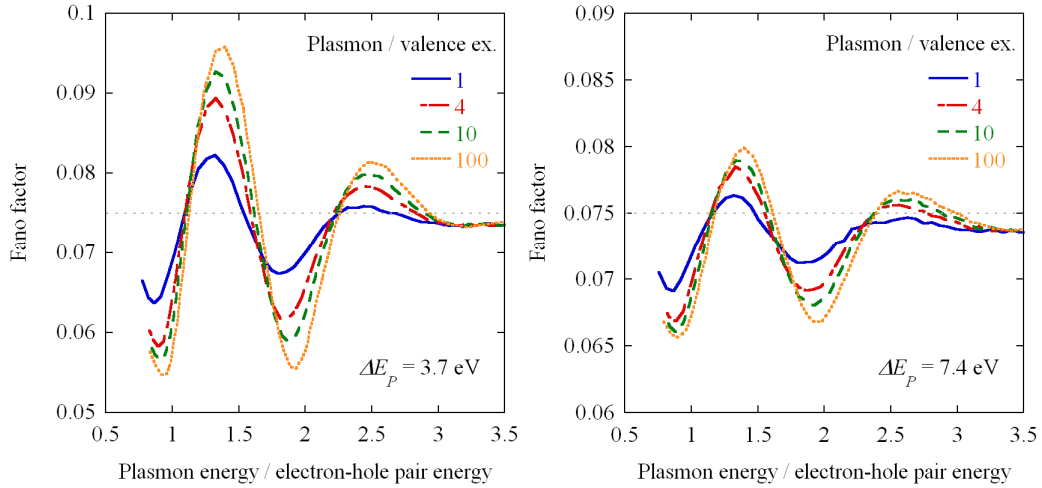
Figure 15. Fano factor vs. plasmon energy (in units of pair energy) for plasmon FWHM equal to 1 (left panel) and 2 (right panel) times that of silicon. The bandgap is set to 5 eV. The valence band is assumed uniform and equal in width to the bandgap, and the incident energy is 10 keV. Different curves represent different likelihoods of plasmon vs. valence excitation at higher-energies. The horizontal line is the result when a uniform DCS is used.

A possible explanation is related to the average electron-hole pair energy w in these simulations, which is the difference in the mean energy of terminal electrons (with energies less than a bandgap width above the bottom of the

55

conduction band) and that of terminal holes (with energies within a bandgap width below the top of the valence band). Comparing the minima in Figure 15 to the mean pair energies at these points, the minima occur at plasmon energies a bit lower than integer multiples of the mean pair energies. At the minima near $2w$ for example, each plasmon decay would be likely to result in 2 electron-hole pairs relative to any other number, resulting in a more deterministic process.

It is interesting to note that the Fano factor for higher plasmon energies in Figure 15 approaches values within a few percent of that for a uniform DCS, where any energy-loss is equally probable in a given event. That a DCS with a high plasmon energy and a flat DCS produce very similar results is consistent with the hypothesis that energy resolution is determined by low energy-loss processes.

Given the above result, the variation of energy resolution with the valence band width is investigated using a flat DCS, where E_V/E_G is the only free parameter (Figure 16). The Fano factor is at a minimum for very narrow valence bands, approximating molecular levels, and also goes through a minimum when it is approximately twice the band gap. It is plausible that under these conditions electron energy is likely to be reduced in more discrete units leading to a reduced variance. That both F and w are lower for narrow valence bands can be understood intuitively, given that electrons and holes are allowed to relax toward the bandgap until constrained by energy conservation. At the end of the electron cascade all simulated electrons are between the conduction band minimum and E_G above the conduction band minimum. All holes will be within E_G of the

56

valence band maximum. For $E_V \geq E_G$, an individual electron-hole pair can have

an energy w_i in the range $E_G \leq w_i \leq 3E_G$, whereas in the limit $E_V \to 0$

$E_G \leq w_i \leq 2E_G$. Clearly, the average pair energy should be lower in the second

case. Less variation in w_i is expected to result in a more deterministic

partitioning of the incident energy into electron-hole pairs and therefore a lower

Fano factor. The cusp in $w(E_V/E_G)$ at $E_V/E_G = 1$ is probably due to the onset of

relaxation of holes within the valence band.
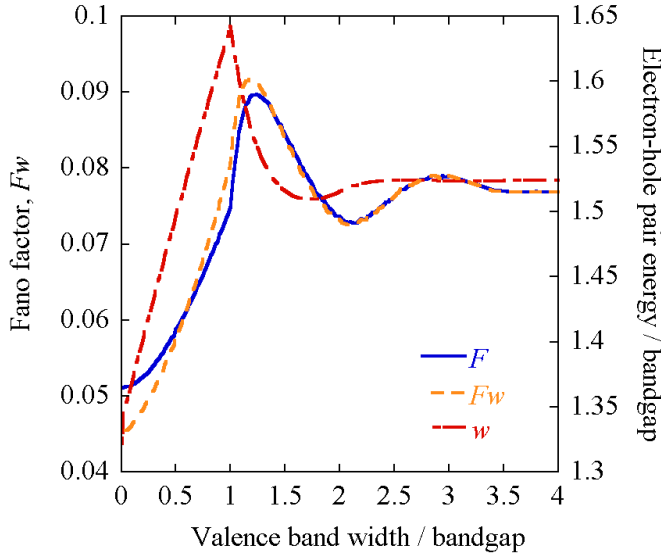
Figure 16. Fano factor (F), average electron-hole pair energy (w), and product Fw plotted against valence band width, in units of the bandgap. F remains constant after 4 eV. The product Fw, which is proportional to the square of the intrinsic energy resolution, is divided by 1.5243, the assymptotic value of w, so it can be plotted on the same scale as F.

4.9.2 Silicon

Although silicon is normally used to detect lower-energy X-rays and charged

particles rather than gamma-rays, we present results for the Fano factor and the

average electron-hole pair energy for comparison with previous simulations and

measurements. The creation of electron-hole pairs in silicon is simulated by

setting our model parameters to the following values: $E_P = 16.7$ eV, $\Delta E_P = 3.7$

eV, and $E_F = 12.78$ eV [7]. Using the EELS spectrum shown in Figure 7 as a

guide, values of $\alpha \sim 2$ and $W_P \sim 1$ are assumed, though these values may change

as better spectra become available. The valence band density-of-states was

calculated using the density functional Layer Korringa Kohn Rostocker (LKKR)

code of Maclaren[47] (Figure 17). Inner shells are included here, even though

they will have little effect. By our estimation (§4.6), scattering by optic phonons

will have a minimal if not negligible effect, and they are not included in the

simulations for silicon. The calculated inverse mean-free-paths (IMFPs) and

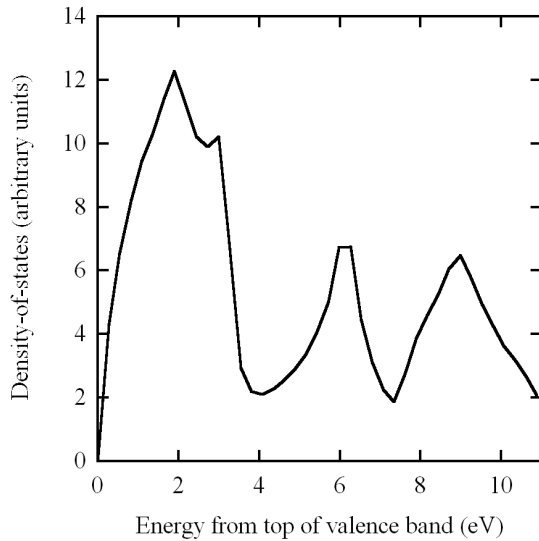angle-integrated differential IMFPs (DIMFPs) for silicon are shown in Figure 18.

Figure 17. Valence band density-of-states for silicon calculated by LKKR.
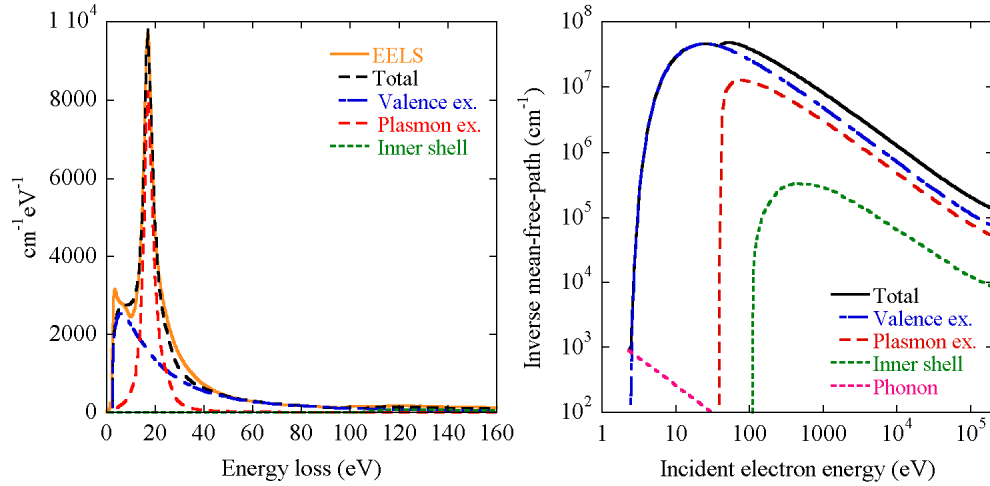Energies are with respect to the top of the valence band.

Figure 18. Silicon differential (left) and total (right) inverse mean-free-paths for inelastic electron scattering processes.

Choosing a value for the effective bandgap is a complicated issue and requires some thought. At low temperatures, silicon has a minimum indirect bandgap of 1.15 eV[7]. In our code it is assumed, optic phonons aside, that any electron that is allowed by energy conservation to produce an additional electron-hole pair will do so. Using the minimum indirect bandgap, 1.786 eV is calculated for the average electron-hole pair energy, a bit higher than the value of 1.5 E_G quoted by Alig[5] for parabolic bands. Incorporating the model for optic phonon emission from §4.6 adds 0.05 eV. This is much lower than the measured average electron-hole pair energy of 3.73 eV[21]. The use of the minimum indirect bandgap with our simplified model therefore appears to be insufficient.

A more realistic estimate of the effective bandgap might be found by calculating the average indirect bandgap over the entire Brillouin zone. Using the VASP density functional code[37, 38] we obtained a value of 2.323 eV, and this becomes ~ 3.0 eV after correcting for the well known underestimation of

59

bandgaps by DFT-LDA. For $E_G = 3.0\,\text{eV}$, the average electron-hole pair energy

is now 4.91 eV, much greater than the experimental measurement.

The models used by Fraser[7] and Gao[8] use 2.56 and 2.5 eV respectively

for the minimum possible energy loss, and both calculate mean pair energies in

agreement with the accepted $\sim 3.7\,\text{eV}$. Both optical[44] and electron energy loss

data show the minimum energy loss is identical to the band gap. Energy loss

spectra can be used to measure the effective bandgap for semiconductors only if

the zero loss peak is subtracted accurately. It is essential to not only record

spectra from thin areas to minimize multiple scattering effects but also to use field

emission microscopes (and maybe monochromators as well) to accurately record

the low loss region.

Following Fraser[7] and Gao[8], an effective bandgap of 2.5 eV results in

$w = 4.01\,\text{eV}$ with our simulation, which is still too high. It is possible that w is

lower for Fraser[7] and Gao[8] due to their treatment of plasmons. Both assume

16.6 eV plasmons that always result in 5 electron-hole pairs giving 3.32 eV per

pair. Given the assumptions stated at the beginning of this section, we calculate

the mean pair energy and the Fano factor for a range of effective bandgaps

(Figure 19). The shape of the valence excitation PDF (4.15) is (approximately)

maintained by scaling ΔU_{peak} inversely with the bandgap and "tail parameter" B

proportionally with the bandgap. We proceed using an effective bandgap of 2.3

eV which yields 3.66 eV for the average electron-hole pair energy. Results for

incident electron energies ranging from 10 – 10,000 eV are plotted in Figure 20

along with results assuming a uniform DCS and a uniform valence band DOS.
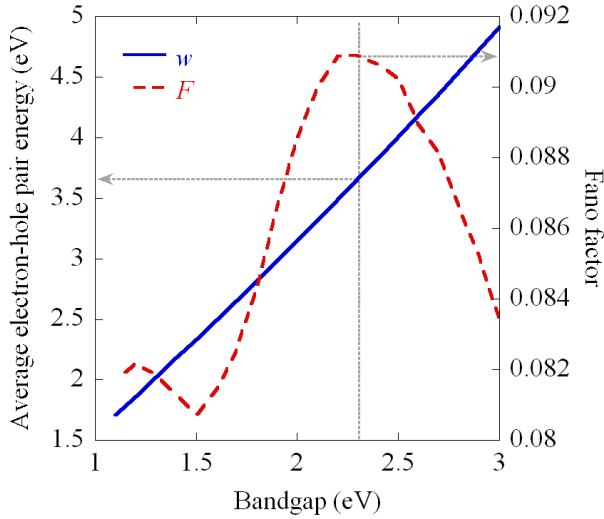
Figure 19. Mean electron-hole pair energy (solid curve) and Fano factor (dashed curve) against effective bandgap in silicon for 3 keV electrons (see text).

Figure 20. Fano factor vs. incident electron energy for silicon using a measured EELS spectrum and a calculated valence band density-of-states (DOS) (solid curve). Also shown are results using a uniform energy-loss DCS (dashed curve), a uniform valence band DOS of width ~11 eV (dot-dashed curve), and both a uniform energy-loss DCS and a uniform valence band DOS (dotted curve).

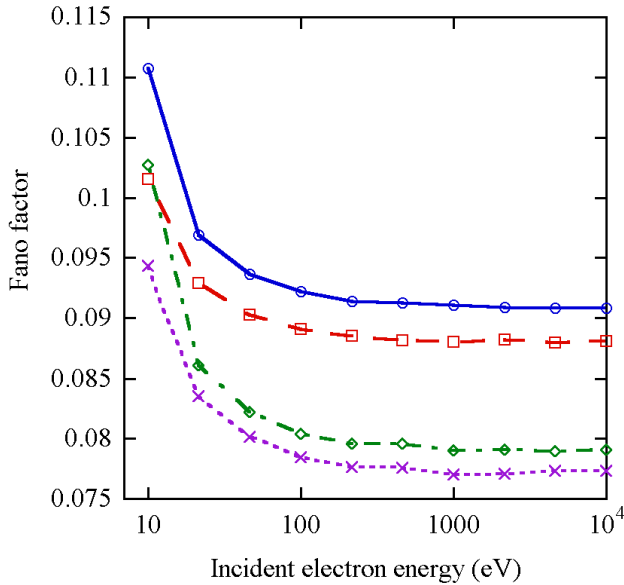From Figure 20 it is seen that the Fano factor is slightly higher for a differential cross section constructed according to our model than for flat, uniform differential cross section. F is also slightly greater when the LKKR valence band density-of-states [47] is used rather than a uniform density-of-states. These Fano factors are only several percent apart, and our result for silicon represents a modest departure from the high E_V/E_G limit of Figure 16. Along with Figure 15, this demonstrates the existence of regimes where attributes of the DCS have little effect on F. That F saturates around a few keV is consistent with the results of Gao[8].

Our calculated value of $F = 0.091$ is lower than that obtained by others who have recently developed similar Monte Carlo codes. For example, Gao[8] and Mazziotta[48] have calculated values of 0.134 and 0.117 respectively. Measured values for F in silicon vary, but many are in the range $0.12 - 0.16$[21-23]. Papp[24], on the other hand, measured $F = 0.067$, significantly lower than our result. The higher values of F calculated by some authors may be due to optic phonons. As mentioned in section 4.6, Fraser[7] and Gao[8] use a mean-free-path of 6 nm for emission of optic phonons for electrons of energy 5 eV relative to the valence band maximum. When we include optic phonons using their mean-free-path (4.48), we calculate $F = 0.110$. This also has the consequence of increasing the average electron-hole pair energy to 4.28 eV.

5   Cascade in a Gamma-ray detector

As gamma-rays pass through matter, they are usually either totally absorbed, in the case of photoelectric ionization, or scattered well out of the beam in a single interaction. This is in contrast with the more continuous energy loss experienced by massive particles. The number of photons per second in the beam N decreases exponentially with depth in the material. If n is the number density of atoms and there is a cross-section σ for interactions with each atom, the number of interactions per second in a slab of material with thickness dx is

$$-dN = Nn\sigma dx \tag{5.1}$$

Integrating, we have

$$N = N_0 e^{-n\sigma x} = N_0 e^{-\mu x} \tag{5.2}$$

where N_0 is the initial flux of photons. Attenuation coefficient or inverse mean-free-path (IMFP) $\mu \equiv n\sigma$, as defined in §4.[2]

The four relevant processes are photoelectric absorption (μ_{PE}), Compton scattering (μ_C), and electron-positron pair production (μ_{PP}), and Rayleigh (coherent) scattering (μ_R). Each process can be associated with its IMFP, and these are simply added to obtain a total attenuation coefficient $\mu = \mu_{PE} + \mu_C + \mu_{PP} + \mu_R$ for gamma interactions[2]. IMFP's from the LLNL database[30] for these processes in silicon, germanium, and lead are plotted for $10 - 10^7$ eV photons in Figure 21 along with total inelastic IMFPs. In our simulations photon processes, along with Bremsstrahlung radiation and elastic electron scattering, are handled by the Penelope radiation transport code, and for

63

that reason are only briefly summarized here. More information on the treatment

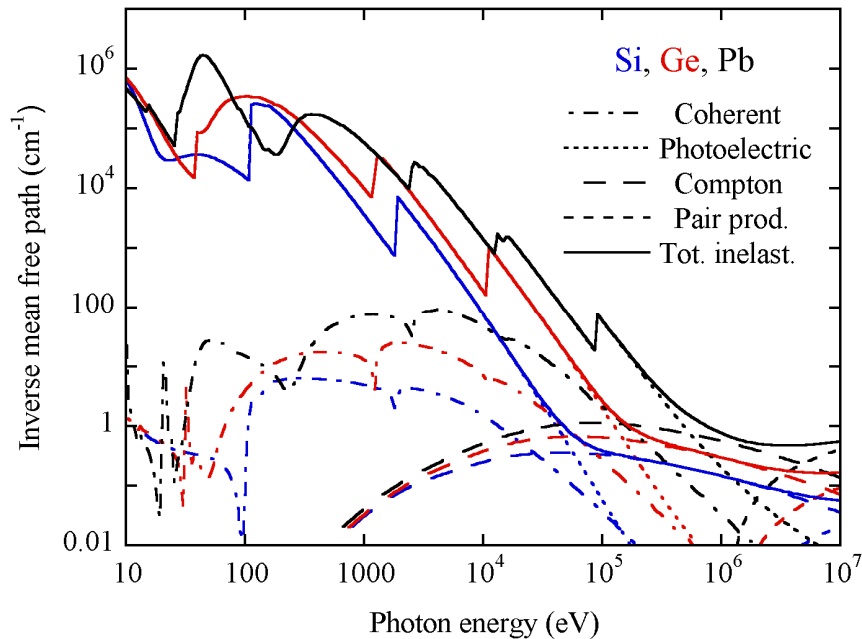of these processes can be found in the Penelope documentation[29].

Figure 21. Inverse mean-free-paths (IMFP's) for relevant photon processes: Rayleigh (coherent) scattering, photoelectric ionization, Compton scattering, and electron-positron pair production in silicon, germanium, and lead. The total inelastic IMFP, the sum of photoelectric, Compton, and pair production IMFP's, is also shown.

The Penelope[16] radiation transport code is capable of calculating

trajectories of electrons, photons, and positrons through materials whose

geometry can be specified by the user. On its own, this Fortran 77 code is well

suited for problems along the lines of calculating distributions of backscattered

and transmitted particles, and determining radiation doses.

To speed up simulations of high-energy particles, Penelope uses mixed

simulation algorithms where there is a distinction made between "soft" and

"hard" interactions for electrons (and positrons). The former represents low-loss,

small-angle scattering events which are described by probability density functions for both energy-loss and scattering angle incorporating multiple events. "Hard" interactions are treated individually. Since the objective here is to count the electrons and holes generated in each shower, soft elastic interactions are allowed, but not soft energy losses, since these would drain energy that could be partitioned into electron-hole pairs. This is controlled in Penelope via several input parameters. Parameter $C_1 \approx 1 - \langle \cos \chi \rangle$ is related to the total deflection χ from multiple "soft" interactions and C_2 is the maximum fractional energy loss $(\Delta E / E)$ tolerated for soft inelastic scattering. Only "hard" interactions with losses greater than cutoff values W_{CC} and W_{CR} are simulated, where the latter is for Bremsstrahlung radiation and the former ionization processes. W_{CR} is set to the lowest value allowed by Penelope, which is 10 eV for the 2005 version. The parameter values used in this work are listed in Table 2.

Table 2

Values for Penelope parameters.

Parameter	Value
C_1	0.05
C_2	0
W_{CC}	0
W_{CR}	10 eV

5.1 Photoelectric absorption

Photoelectric absorption describes the absorption of a photon which ionizes an atomic electron. Due to energy conservation, the energy of the ejected electron

will be that of the incident gamma minus the electron's binding energy. This leaves the atom in an excited state. As electrons relax to lower shells one or more characteristic X-rays are emitted. In some cases the X-ray's energy will be transferred to an outer shell electron which is ejected. Such ejected electrons are known as Auger electrons. The attenuation coefficient or IMFP for photoelectric absorption is roughly proportional to $\mu_{PE} \propto nZ^5 E_\gamma^{-3}$. Photoelectric absorption is then most important for targets composed of heavy elements or for lower-energy gamma-rays. Only for very high atomic numbers is it relevant for MeV photons.[2]

5.2 Compton scattering

Compton interactions involve the scattering of a photon by an electron whose binding energy is much less than E_γ. In this case the electrons are effectively free particles, and momentum conservation prevents the gamma-ray from being completely absorbed. For photon energies much less than the rest energy of an electron (511 keV) the photon looses little energy. At the opposite extreme, the gamma-ray transfers most of its energy to the electron. Since the target electrons are effectively free, one expects the IMFP to be proportional to the density of electrons in the material. The IMFP is vaguely described as $\mu_C \propto nZ/E_\gamma$, though it is really much more complicated. The scattering of gamma-rays by a free electron at rest is described by the Klein-Nishina differential cross section[49], and the treatment in Penelope considers the momentum of atomic electrons[29]. Compton interactions are often the primary means of energy loss for gamma-rays

with energies well above the K-shell binding energy but less than a few MeV

where pair production becomes important.

Compton scattering leaves a distinctive feature in gamma-ray spectra, and

this will be demonstrated later (§6). A "Compton edge" is observed, which

corresponds to the maximum energy the incident photon can lose when scattered

by an electron. The prominence of this feature is due to the fact that the IMFP for

fast electrons is orders of magnitude greater than that for photons of a similar

energy (compare Si in Figure 18 and Figure 21), so the scattered photon may

escape the detector, whereas most of the electron's energy is likely to be

deposited. A cutoff energy-loss for a photon incident on a free electron at rest can

be calculated considering energy and momentum conservation. For a photon of

initial energy E_γ, the ratio of final to initial photon energies is[2]

$$\frac{E'_\gamma}{E_\gamma} = \left[1 + \frac{2E_\gamma}{m_0 c^2}\right]^{-1} \tag{5.3}$$

where $m_0 c^2 = 511\,\text{keV}$ is the rest energy of an electron. Solving for the

deposited energy $\Delta E = E_\gamma - E'_\gamma$, the Compton edge should be seen at an energy

$$\Delta E = E_\gamma \left(1 - \left[1 + \frac{2E_\gamma}{m_0 c^2}\right]^{-1}\right). \tag{5.4}$$

5.3 Pair production

In electron-positron pair production the energy of a gamma-ray is partitioned into

the rest and kinetic energies of an electron and positron. This process is therefore

only possible for gammas in excess of $2m_e c^2 = 1.02\,\text{MeV}$ (twice the electron rest

energy), and will not become a dominant process until at least a few times that[2, 18]. Near threshold[2],

$$\mu_{PP} \propto nZ^2(E_\gamma - 2m_e c^2).$$ (5.5)

As the positron slows down it will annihilate with an electron. This results in two 0.511 MeV gamma-rays, either of which may escape the detector. For this reason pair production can create a unique signature in the detector response [2, 18]. Pair production is important for gamma energies generally higher than the range of interest here, so we will not be concerned with pair production hereafter.

5.4   Rayleigh scattering

Rayleigh (coherent) scattering is an elastic process where photons interact with bound electrons without causing ionization. The incident photon changes direction but does not lose an appreciable amount of energy. Rayleigh scattering must be included in radiation transport codes to calculate trajectories, but is expected to have little effect on the electron cascade.[18]

5.5   Bremsstrahlung radiation

Bremsstrahlung radiation, or braking radiation, occurs when a charged particle is deflected, in our case due to the electrostatic field of the atoms in the detector material. Any charged particle can be subject to Bremsstrahlung radiation, but it is much more prevalence for electrons and positrons than for heavy charged particle such as ions. The spectrum of possible energies for the emitted photons varies smoothly from zero to the energy of the charged particle. [29, 50]

5.6 Elastic electron scattering

In elastic scattering, an electron (or positron) is deflected by an atom that is left in its initial quantum state. Since the target recoils, a finite amount of energy is lost but this is usually a small enough loss that it can be taken as negligible. In our simulations with Penelope, this energy loss is neglected, which amounts to taking the atomic nucleus as infinitely more massive than an electron. [29]

6   Simulation of Gamma-ray Detectors

The production of electron-hole pairs by mono-energetic gamma-rays is simulated

by incorporating our model for inelastic electron scattering from §4 into the

Penelope radiation transport code. A slightly modified version of the driver

routine "pencyl" is used, and the input geometry (Figure 22) consists of a

cylindrical detector with photons striking one face at normal incidence. Each

shower is initiated by a single photon of a given energy, and the showers are

binned by the number of electron-hole pairs produced in the material. If the bins

are scaled such that the maximum of the full-energy peak matches the energy of

the initial gamma-rays, a histogram is produced which can be compared to a

measured detector response function. The full-energy peak, or photo-peak, refers

to the feature in the detector response function which corresponds to showers

where the full energy of the incident particle is deposited. These histograms show

escape peaks, where X-rays from atomic relaxation escape the detector material.

These are labeled according to the responsible atomic transition with

spectroscopic notation, where Kα represents an electron with principle quantum

number $n = 2$ (L shell) relaxing to $n = 1$ (K shell), and Kβ and Kγ respectively

refer to transitions from $n = 3$ (M) and $n = 4$ (N) to $n = 1$. In the following

subsections we continue with silicon, in the context of X-ray detection. In the

subsequent four subsections two more semiconductors, gallium arsenide and zinc

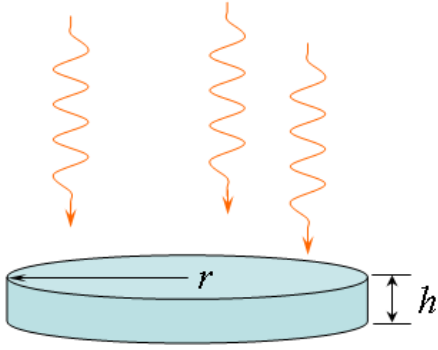telluride, and two scintillators, cerium fluoride and LSO are considered.

70

Figure 22. Input geometry for simulating gamma-ray detectors with Penelope. The radius and height of the cylinder are varied for different materials. Incident photons approach the detector at normal incidence and are randomly distributed on one face of the cylinder.

In each case EELS data is used along with a calculated valence band density-of-states as in §4.9.2. With the exception of silicon, the EELS data was obtained using the Tecnai F20 electron microscope with a Gatan imaging filter at Arizona State University. For GaAs, ZnTe, and CeF$_3$ the density-of-states was obtained using the VASP[37, 38] DFT code, and for LSO it is primarily taken from Wei et al.[51]. Binding energies for inner shells with $E_B < 150$ eV are based on X-ray photoelectron spectroscopy data (XPS or ESCA) from [52] and fitting EELS spectra where applicable. Since the scintillators have wide bandgaps and relatively narrow valence bands compared to semiconductors, plasmons are not well defined in the free-electron gas model used here. Plasmon excitation is therefore omitted from the inelastic scattering model for the scintillators.

6.1 Silicon X-ray detector

The simulation of a silicon X-ray detector represents a departure from the motivation of homeland security concerns, as its low atomic number makes it more useful for detecting X-rays than the gamma-rays in the energy range of

71

interest in radioactive decays. Fraser[7], for example, simulates $0.05-10$ keV

X-rays and describes the need for such simulations in the context of X-ray

astronomy.

The model parameters for inelastic electron scattering from §4.9.2 are

used here (phonon scattering is neglected), and we consider a silicon disk with

radius and thickness 5 mm. For the purpose of comparison with experiment, the

X-ray spectrum due to a ^{55}Fe radioactive source is simulated (Figure 23), as this is

commonly used to evaluate X-ray detectors. It can be assumed that ^{55}Fe always

decays to stable ^{55}Mn by electron capture[53]. The resulting Mn-Kα and Mn-Kβ

X-rays are simulated, which have energies 5.89 and 6.49 keV and probabilities

per decay of 24.5% and 3.38%[53]. It is the ratio of probabilities

$p(K\beta)/p(K\alpha) = 0.138$ that is required for our purposes. The histogram from the

simulation is plotted with experimental data from [24] by aligning the simulated

histogram with the data at maximum of the Mn-Kα peak. In Figure 24 only the

Mn-Kα peak is shown. The histograms representing the simulated detector

response are binned to improve their appearance. The size of the simulated

energy-bins in Figure 23 is 5w (18.3 eV) and for Figure 24 it is 2w (7.3 eV) where

$w = 3.66$ eV is the average electron hole pair energy. We underestimate the

magnitude of the Mn-Kβ peak relative to Mn-Kα, and it is hard to imagine how

this could happen since more than 99% of the showers are deposited in the

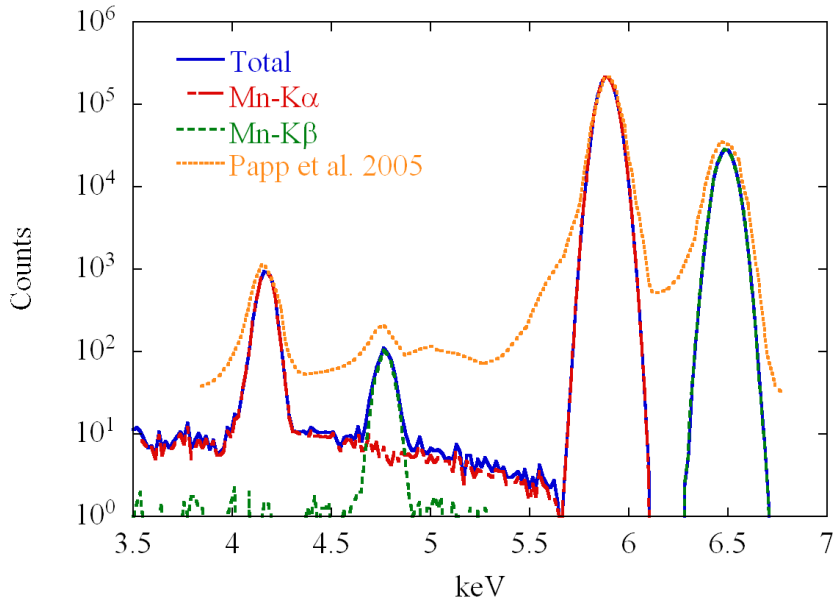Mn-Kα and Mn-Kβ peaks. It would seem that $p(K\beta)/p(K\alpha)$ must not match

the experiment from [24].

Figure 23. Simulated response of a 5 mm thick silicon detector to a [55]Fe radioactive source compared with experimental data from Papp et al. (2005). Characteric X-rays with energies 5.89 and 6.49 keV were simulated.
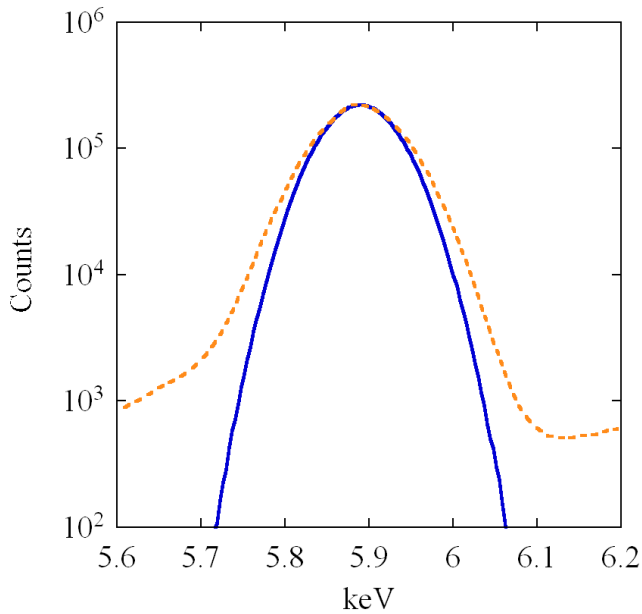

Figure 24. Simulated peak due a Mn-Kα X-ray (5.89 keV) incident on a 5 mm-thick silicon detector compared with experimental data from Papp et al. (2005).

It is expected that the simulated detector response will generally differ

from the measured response since the only the statistics of electrons-hole pair

creation are simulated, whereas experiments include the effects of electron noise and incomplete charge collection (see equation (3.19)). Low-energy tailing due to incomplete charge collection is visible in both full energy peaks from [24]. Without our modifications to Penelope, it would still be possible to produce response functions that could be compared to experimental data, but the intrinsic width of the full-energy and escape peaks due to the statistics of electron-hole pair creation would not be reproduced. As in §4.9.2, we calculate $F = 0.091$ for $w = 3.66$ eV.

6.2   Gallium Arsenide

Gallium arsenide (GaAs) has been used as a radiation detector for decades, although charge collection issues[18] limit detector thickness and therefore its detection efficiency for gamma-rays. At room temperature GaAs has a minimum bandgap of 1.43 eV[25], which means it can potentially be used without cooling. GaAs detectors also perform well where radiation damage effects are concerned[18].

The EELS spectrum for GaAs is shown in Figure 25 along with the applied inelastic electron scattering model. Modeling this data is somewhat more complicated than for silicon (§4.9.2) because the M_{45} atomic shells in both gallium and arsenic have IMFPs comparable to the plasmon and valence excitation components, and furthermore the Ga M_{45} subshell has a binding energy of ~18 eV[52], which makes it difficult to distinguish from the plasmon

contribution. The model from §4 is therefore applied to the EELS data in a more formal way using $\chi^2 - \text{minimization}$.
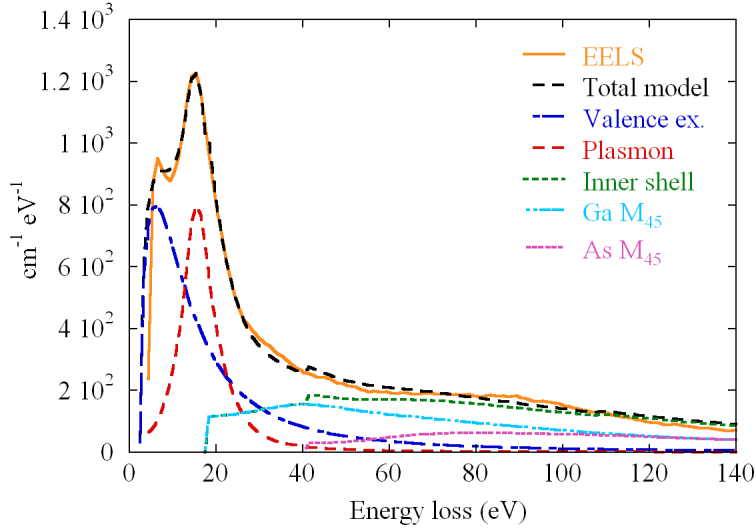

Figure 25. Low-loss EELS spectrum and inelastic electron scattering model for GaAs.

The following model function is applied to the EELS spectrum:

$$J(\Delta E) = P(\Delta E, E_P, \Delta E_P, C_P) + S(\Delta E, B, C_S) + A(\Delta E, C_A) \qquad (5.6)$$

P, S, and A represent the plasmon excitation, single valence electron excitation, and atomic shell ionization components respectively. The parameters allowed to vary in the fit are plasmon energy and width E_P and ΔE_P, valence excitation "tail parameter" B (see §4.4), and overall amplitude constants C for each component. $J(\Delta E)$ is calculated for each energy loss bin in the EELS data greater than a few eV, and each data point used in the fit is weighted by the Poisson variance for that bin, which is equal to the number of counts before zero-loss peak subtraction and deconvolution. The valence excitation parameter

75

ΔU_{peak} is estimated visually in order to constrain the fit, and the plasmon

dispersion parameter $\alpha = 2$ as in silicon.

The density-of-states used for simulating GaAs is shown in Figure 26.

The feature primarily due to the As-4s subshell is separated by a few eV and is

not considered part of the valence band for our purposes. The contribution to the

EELS spectrum is difficult to determine since it is superimposed with the much

stronger valence and plasmon excitation components. For this reason the As-4s

subshell is omitted in our analysis of the EELS data, though a level corresponding

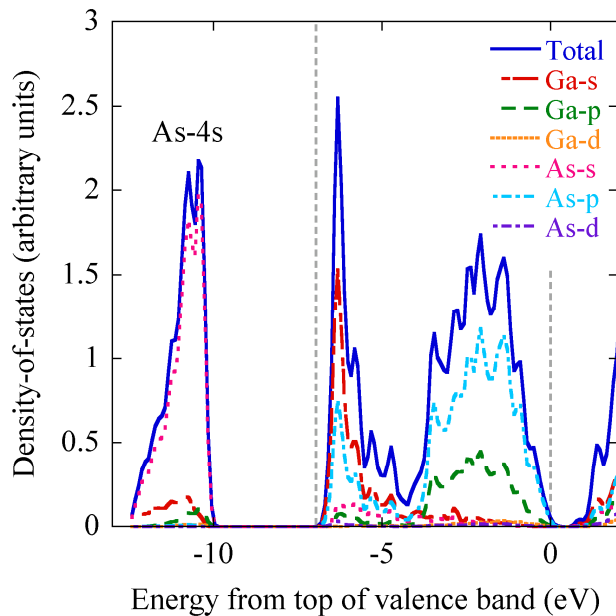to As-4s is included in Penelope's treatment of atomic relaxation.

Figure 26. GaAs density-of-states calculated using VASP DFT code. The As-4s
electrons are not included as part of the valence band.

The total IMFPs as calculated by our inelastic electron scattering model

are shown in Figure 27. Comparing this with the IMFPs for silicon (Figure 18)

and optic phonon energy-loss functions in Figure 14, it is clear that phonon

scattering is much more significant in GaAs, though still only relevant for electrons of energies within several eV of the band gap. The mean-free-path for phonon scattering is 0.14 μm for electrons with energy 4 eV relative to the conduction band minimum in GaAs versus ~20 μm in silicon.
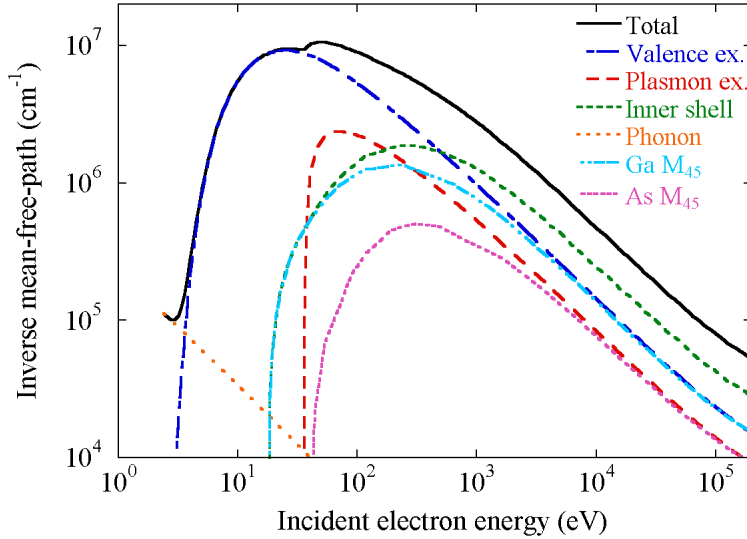

Figure 27. Model inverse mean-free-path for GaAs.

The effective bandgap used for GaAs is determined in the same way as for silicon (§4.9.2). The average electron-hole pair energy has been measured to be 4.2 eV[25], and this result is obtained with a 2.4 eV effective bandgap. Figure 28 shows the effect of changing the effective bandgap on *w* and *F*.
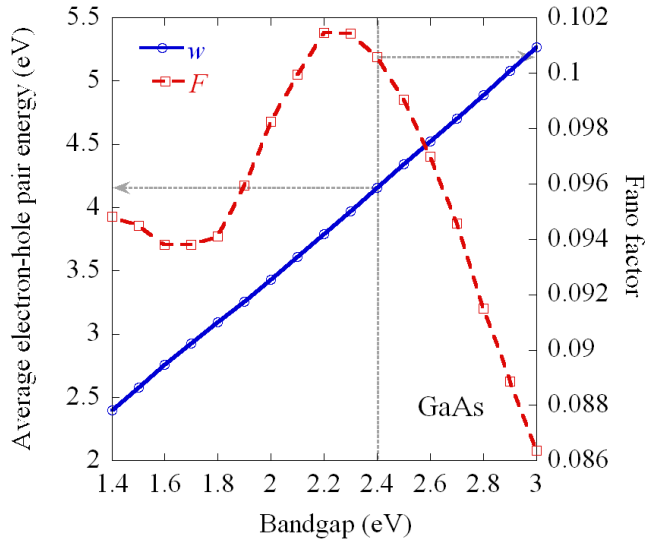
Figure 28. Average electron-hole pair energy (solid curve) and Fano factor (dashed curve) against effective bandgap in GaAs for 10 keV electrons. The vertical dotted line marks 2.4 eV, the value for the bandgap chosen to give an average electron-hole pair energy of ~4.2 eV.

To test the accuracy of the modified version of Penelope, a simulation is run to match the X-ray spectrum shown in Owens et al.[54] for a [241]Am radioactive source and a 40 micrometer thick GaAs detector cooled to $-20°C$. As seen in Figure 29, the expected escape peaks are reproduced by Penelope with approximately the correct intensity. The simulation results and data are compared by matching the intensity at the maximum of the full-energy peak. Of the 5.6×10^6 showers simulated, 96% of the X-rays passed through the material without creating any electron-hole pairs, so a much thicker detector would be needed for efficient spectroscopy of gamma-rays. As with Figure 23, simulation results are expected to differ from experiment since error introduced by the detector electronics and incomplete charge collection are not simulated. In addition to broadened peaks, a continuum is present which is not reproduced in simulations.
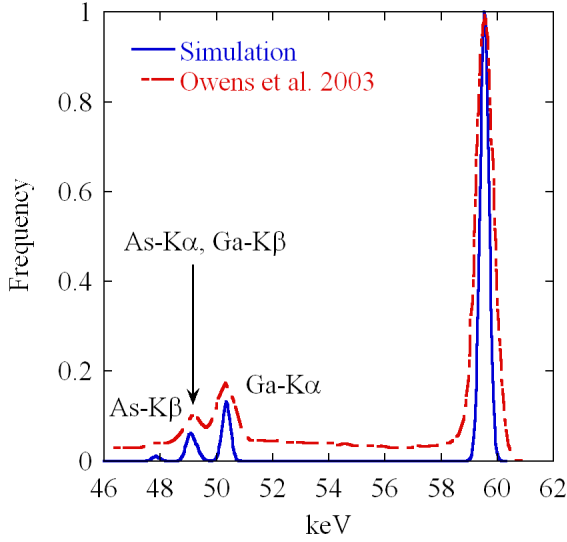
78

Figure 29. Comparison of simulation with measurement for a 40 mm thick GaAs detector. The incident particle simulated is the 59.54 keV x-ray from a [241]Am source. ~5.6 million showers were simulated.

We calculate $F = 0.100$ for an average pair energy $w = 4.144$ eV. F is somewhat less than experimentally determined values from [55] ($F = 0.138 \pm 0.005$ assuming $w = 4.3$) and [56] ($F = 0.12 \pm 0.01$ assuming $w = 4.27$).

6.3 Zinc Telluride

Zinc telluride (ZnTe) is commonly combined with cadmium telluride (CdTe) to produce $Cd_{(1-x)}Zn_xTe$ (CZT), and CZT detectors have achieved commercial production[18]. Increasing the zinc fraction x lowers the lattice constant of the alloy and increases the bandgap. ZnTe is the high-bandgap extreme, with $E_G^{min} = 2.257$ at room-temperature measured in a photoluminescence study[57].

The analysis of the EELS spectrum (Figure 30) for ZnTe involves the same issues as GaAs and is for the most part carried out in the same way. The shape of the Te N_{45} (3d) edge is modified, and this makes the fit of our model to

the EELS data appear more convincing than that for GaAs. The low-loss portion

of the Te N_{45} PDF is effectively stretched along the abscissa by a factor of ~2

which delays its maximum allowing the inelastic scattering model to match the

shoulder seen in the EELS spectrum at ~90 eV. This modification is illustrated in

Figure 31, where all curves other than the initial Te N_{45} PDF are the same as in
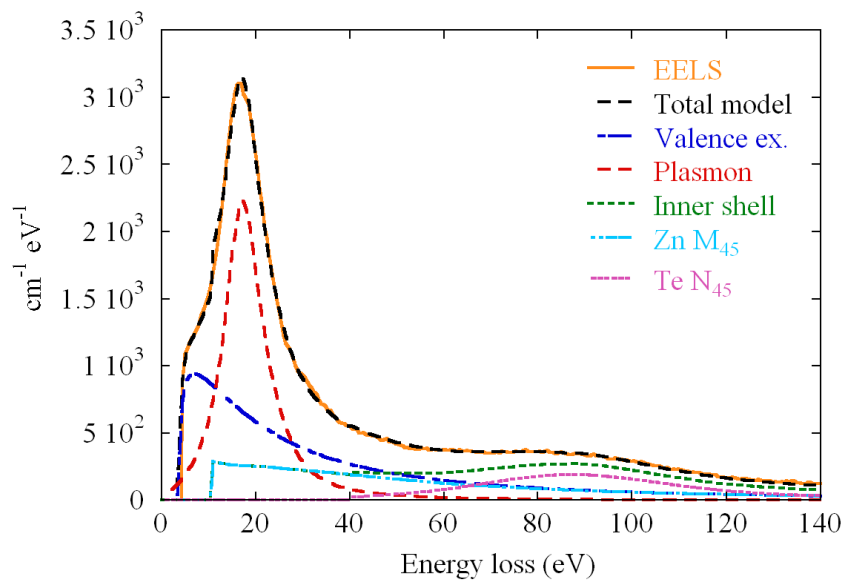
Figure 30.

Figure 30. Low-loss EELS spectrum and inelastic electron scattering model for ZnTe.
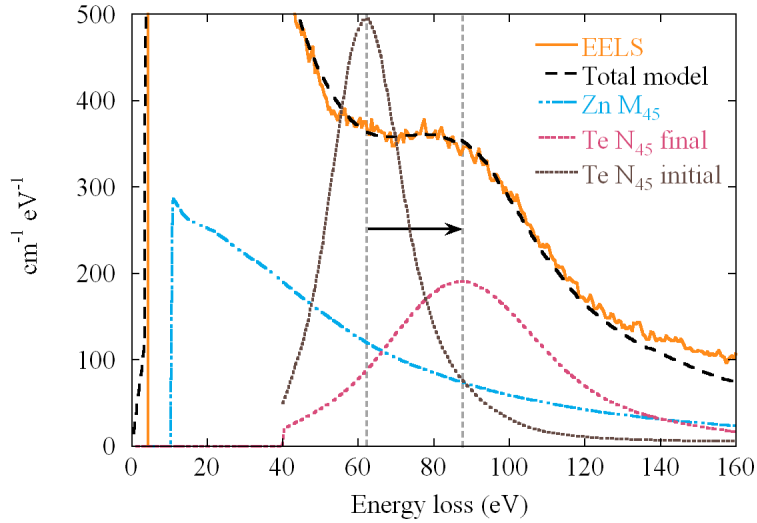
Figure 31. Modification of the Te N_{45} (4d) edge to match EELS data for ZnTe. Zn M_{45} is also shown. The initial version of the Te N_{45} energy-loss PDF is scaled to match the normalization of the final PDF.

The calculated valence band density of states is shown in Figure 32, and is similar in appearance to that for GaAs aside from the proximity of 3d states (Zn M_{45}) to the valence band. Again, the Te O_1 (5s) electrons are not included in the valence band and they are not given a separate PDF in our model since the PDF would be hard to separate from the stronger components due to valence and plasmon excitation, and ionization of the Zn M_{45} subshell. The Zn M_{45} subshell is treated as a discrete inner-shell state with binding energy 10.5 eV relative to the effective conduction band minimum. The total IMFPs for ZnTe are shown in Figure 33.
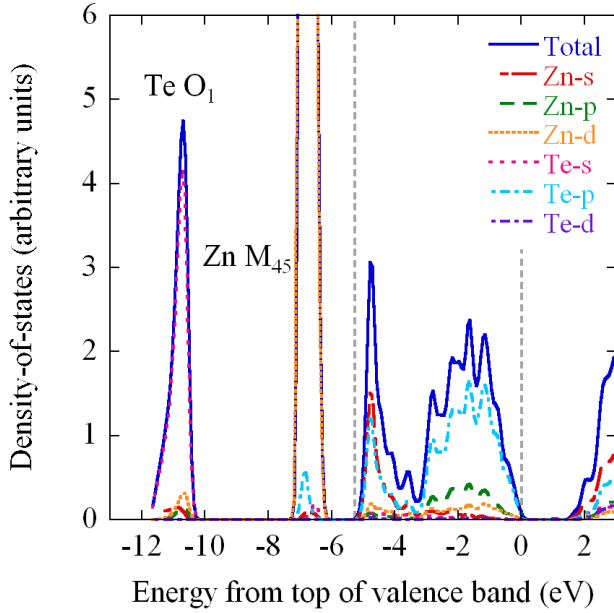
Figure 32. ZnTe density-of-states calculated using VASP DFT code. The Te O_1 electrons are not included as part of the valence band.
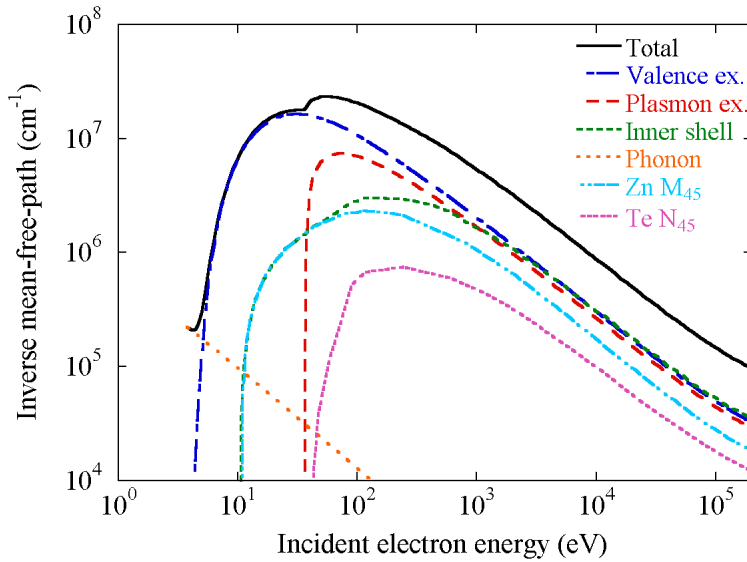

Figure 33. Model inverse mean-free-path for ZnTe.

Although CZT has been thoroughly studied as a radiation detector, there appears to be little work published on the values of w and F in ZnTe, so we do not attempt to choose an effective bandgap that reproduces an accepted electron-hole pair energy w. For want of more information, an effective bandgap $E_G = 3.8$ eV is

chosen based on EELS data and this is may be in error by ~0.5 eV. It is of some

consolation that the ratio of this effective bandgap to the known minimum

bandgap turns out to be approximately equal to the same ratio for GaAs. The

effect of varying the effective bandgap on w and F for 10 keV electrons is shown

in Figure 34.
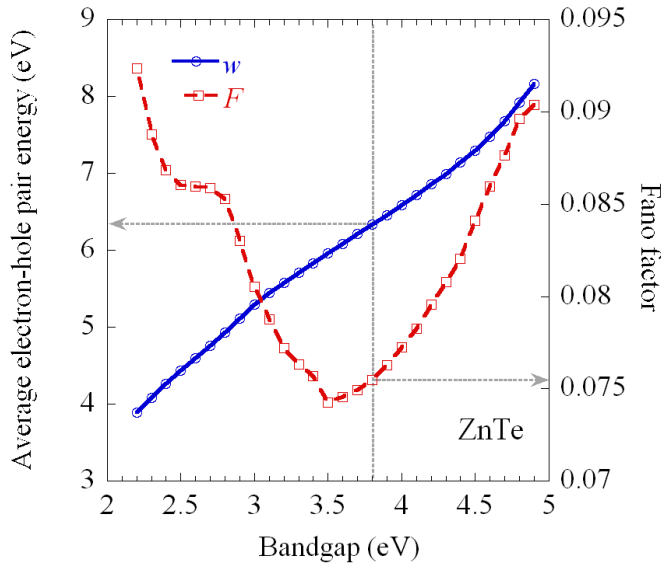
Figure 34. Average electron-hole pair energy (solid curve) and Fano factor
(dashed curve) against effective bandgap in ZnTe for 10 keV electrons. The
vertical dotted line marks 3.8 eV, the value for the bandgap based on the EELS
spectrum.

ZnTe is simulated in the context of gamma-ray detection by considering a

disk of of ZnTe 2mm thick and 1 cm radius, as 2 mm is a typical thickness for a

CZT detector[25]. The simulated detector response for 200 keV gamma-rays is

shown in Figure 35. This simulation gives $w = 6.32\,\text{eV}$ and $F = 0.075$.

Figure 35. Simulated detector response for ZnTe to 200 keV gamma-rays. The right panel shows only the higher-energy bins to reveal more detail in the full-energy and escape peaks.

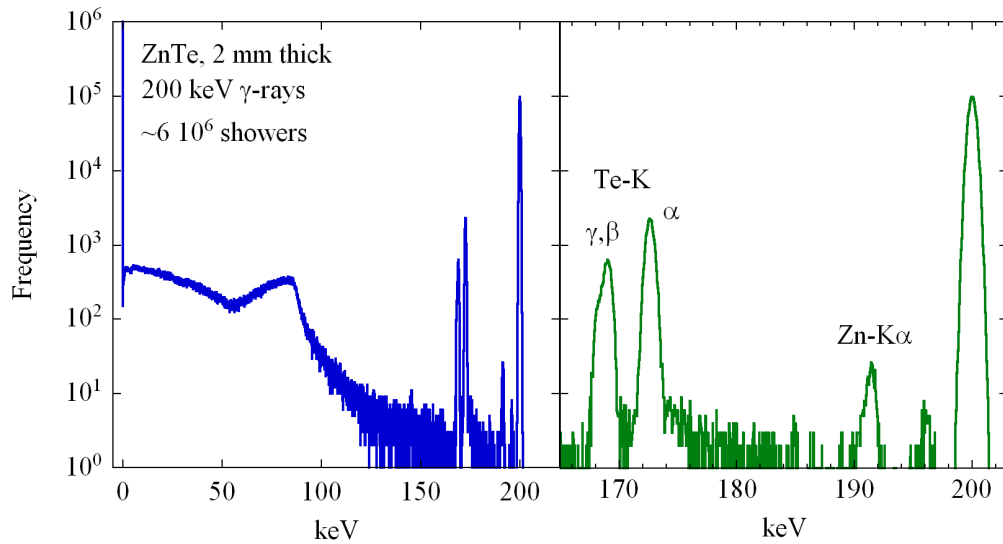## 6.4 Cerium fluoride

Self-doping cerium fluoride (CeF_3) is a scintillator with a relatively low light yield, but is interesting due to its very fast decay time (~5 nanosecond short component and 30 nanosecond long component) and is currently in use for the detection of gamma-rays. The lower-energy portion EELS spectrum is shown in Figure 36 along with the inelastic electron scattering model. The spectrum must be separated into components attributed to the valence band and atomic shells. Considering known atomic binding energies[52], the three peaks in Figure 36 are attributed to, in order of energy, the valence band, and the cerium O_{23} and N_{45} subshells.
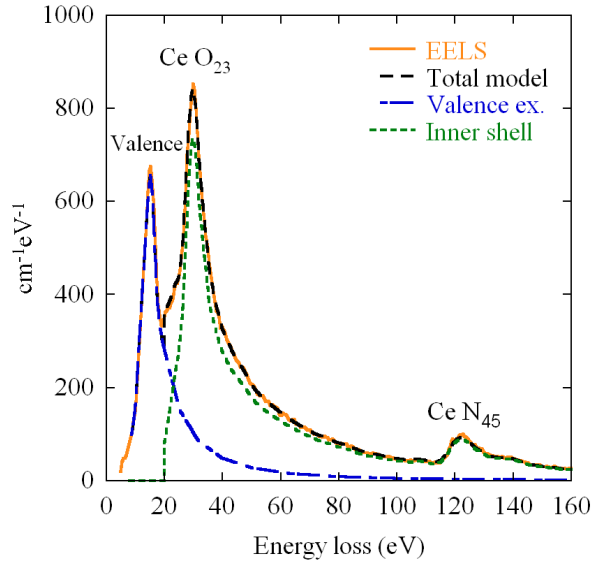
Figure 36. EELS spectrum and inelastic electron scattering model for CeF_3 with prominent features labeled (see text).

Since it would be very difficult to find a theoretical model accurate enough to fit to the EELS data, a simple, pragmatic approach is used to extract energy-loss PDFs for each component. A power-law tail $\propto \Delta E^{-2.5}$ is used to extend the valence excitation component. The corresponding curve appears in Figure 36. This is subtracted from the EELS spectrum. This procedure is repeated on the residual to isolate the $Ce\,O_{23}$ edge, and again to obtain a PDF for the $Ce\,N_{45}$ subshell. The $F\,L_1$ and $Ce\,O_1$ edges, with binding energies 31 and 38 eV [52], should be present in the low-loss region of the spectrum, but are not discernable by eye as they are obscured by the $Ce\,O_{23}$ peak. Using LLNL atomic cross sections[30] as a guide, the $F\,L_1$ plus $Ce\,O_1$ edges (accounting for 3 fluorine atoms per CeF_3 molecule) one estimates that these electrons will contribute ~70% the IMFP of $Ce\,O_{23}$ at 200 keV. Still, a meaningful fit for $F\,L_1$ or $Ce\,O_1$ is unlikely given the lack of features in the EELS data, and atomic data

85

on its own is likely unsuitable in this regime. We therefore "combine" the $F L_1$, $Ce O_1$, and $Ce O_{23}$ subshells, incorporating them as a single energy-loss PDF in our model, which we will refer to as $Ce O_{23}$ hereafter. The remaining inner shells are more tightly bound and result in a weak signals in the EELS data, and these are taken from the Lawrence Livermore database[30].

The valence band density-of-states used for CeF_3, mainly consisting of fluorine 2p states[58], is shown in Figure 37. This calculated DOS approximately resembles DFT calculations and X-ray photoelectron spectra (XPS, or ESCA) from Klier et al.[58]. According to Klier et al.[58], there should be a single electron occupying the Ce-4f orbital, and since these states are responsible for scintillation in CeF_3 we define the effective bandgap between the F-2p valence band and the Ce-5d states. Figure 37 suggests a bandgap of ~8 eV. Since DFT is known to be unreliable in calculating bandgaps we look to experimental data. XPS data[58] suggests a spacing of 3 — 4 eV between the F-2p and Ce-4f states which is less that that from Figure 37, and Wei et al.[59] measure strong absorption attributed to $Ce\ 4f \rightarrow 5d$ upwards of 4.13 eV and calculate 3.96 eV for the corresponding gap. The reflectance spectrum measured by Nisar et al.[60] seems to support an effective gap ~8 eV. An effective bandgap of 8 eV is therefore assumed though this could be in error by ~1 eV.
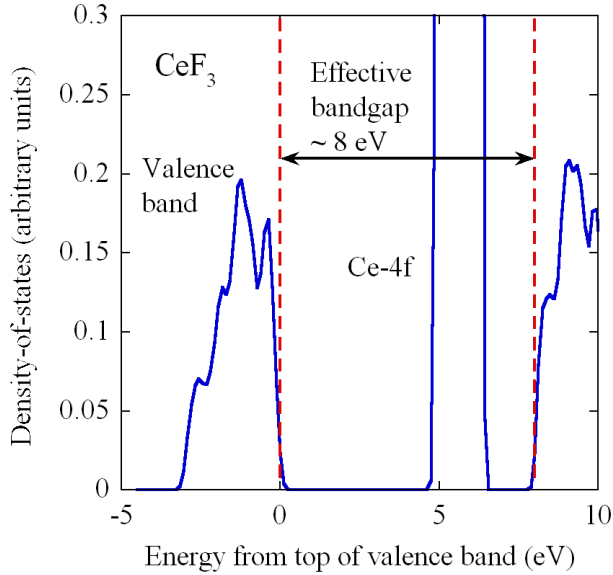
Figure 37. CeF$_3$ density-of-states from VASP DFT code. The feature in the bandgap due to the cerium 4f states, which appears to be overestimated by VASP, is not included in simulations.

It is necessary to calculate total IMFPs (or cross-sections) for the valence, Ce O$_{23}$, and Ce N$_{45}$ PDFs which are consistent with the LLNL data used in our simulations for inner-shell ionization. This is accomplished by integrating the isolated Ce N$_{45}$ PDF (not shown), estimating the total number of counts in the EELS data due to this edge. This feature is chosen rather than the Ce O$_{23}$ edge because it is more isolated in the data and because, being more tightly bound, the atomic data should give a closer approximation to the true cross-section. The Ce N$_{45}$ subshell is assigned a cross-section from the LLNL database at 200 keV, the accelerating voltage of the electron microscope. By summing the counts in the valence and Ce O$_{23}$ components, total cross-sections consistent with the LLNL data are obtained by scaling relative to the Ce N$_{45}$ edge. Total IMFPs are shown in Figure 38.
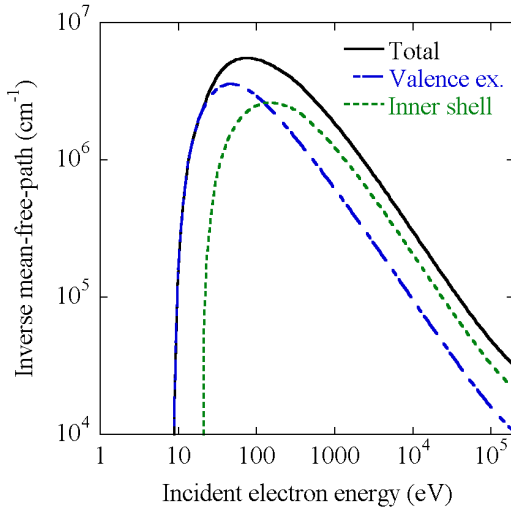
Figure 38. Model inverse mean-free-path for CeF$_3$.

A histogram of the simulated response of CeF$_3$ to 200 keV gamma-rays is shown in Figure 39. The cylindrical geometry has a radius of 3 cm and height 6 cm. The Compton edge (§5.2) is clearly visible. Evaluating equation (5.4) for $E_\gamma = 200 \text{ keV}$, the edge should appear around 88 keV, and this is consistent with Figure 39. This simulation gives $w = 11.59 \text{ eV}$ and $F = 0.046$.
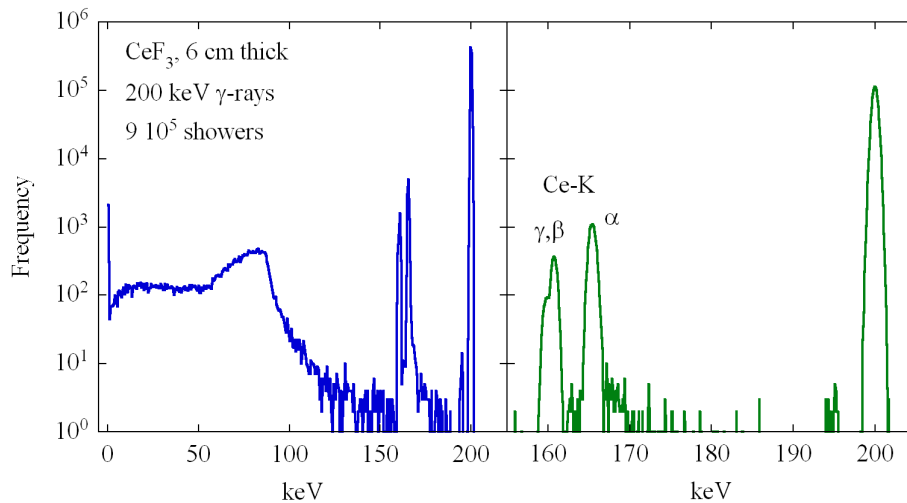
Figure 39. Simulated detector response for CeF$_3$ to 200 keV gamma-rays. The right panel shows only the higher-energy bins to reveal more detail in the full-energy and escape peaks. The frequency is lower on the right-hand side because smaller bins are used.

88

6.5 Lutetium Oxyorthosilicate (Lu_2SiO_5 or LSO)

Cerium doped LSO is an inorganic scintillator with a comparatively high light yield and fast decay time (0.047 μs)[18], and has found widespread use in nuclear medicine such as positron emission tomography (PET) (for example [61, 62]). The EELS spectrum (Figure 40) for LSO is modeled as follows. The peaks at 32 and 41 eV are attributed to the Lu O_3 and Lu O_2 subshells respectively. Based on the cross-sections from the LLNL database[30], the oxygen L_1 subshell should also make a strong contribution. The lutetium O_2 and O_3, and oxygen L_1 subshells are shown separately in Figure 40. As stated by [51], the bandgap of LSO has been determined experimentally to be 6 eV, and this value will be used here.
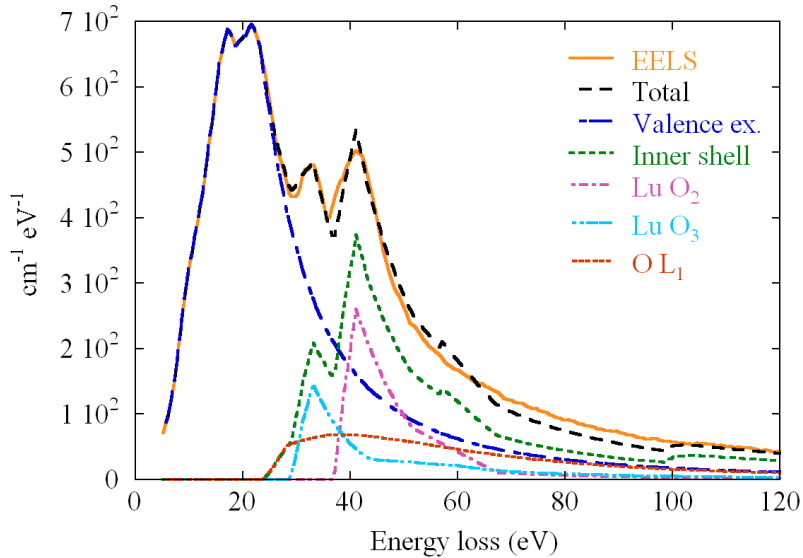

Figure 40. Low-loss EELS spectrum and inelastic electron scattering model for LSO.

Since Lu O_2 Lu O_3, and O L_1 have similar but distinct binding energies, and similar IMFPs, the approach used for CeF_3 is not practical. The valence

excitation component is separated from the EELS spectrum as it was for CeF_3,

and is then subtracted. Calculated PDFs for Lu O_2 Lu O_3, and O L_1, given by

[63-65], are then applied to the residuals. Binding energies from ESCA[52], with

minor shifts to match the EELS spectrum, for Lu O_2, Lu O_3, and O L_1 are 37, 29,

and 24 eV respectively.

These PDFs must be modified in order to construct an adequate model for

the EELS data (Figure 41). First, the profiles of all three components are

modified by superimposing identical PDFs (the initial PDFs from Figure 41)

which begin at a range of binding energies which spans 4 eV. This has the effect

of slowing the onset of the subshell edges and delaying the peaks. The formula

for this operation is
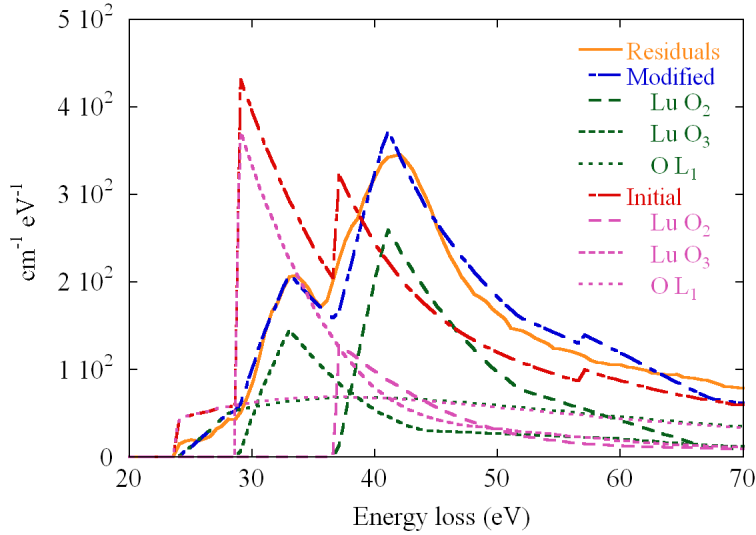

Figure 41. Fitting subshell PDFs to residuals from LSO EELS data, having attempted to remove the valence excitation component. The Lu O_2 and Lu O_3 components are rescaled, and the shapes of all three PDFs are modified (see text).

$$g(x) = \frac{1}{B}\int_0^B f(x-B)\theta(x-B)\,dB\,, \quad x \equiv \Delta E - E_B \qquad (5.7)$$

90

where f and g are the initial and modified PDFs, and θ is the Heaviside step function, which is equal to zero if the argument is less then zero and equal to one if the argument is greater than zero.

An additional modification is made to the Lu O_2 and Lu O_3 PDFs. These PDFs are rescaled by factors of 2.5 and 0.5 respectively over $E_B < \Delta E < E_B + 15$ eV to approximately match the EELS residuals, and then linearly interpolated to their values at $E_B + 30$ eV. The corresponding IMFPs are rescaled to account for the additional area added under the PDFs. In Figure 41 the unmodified Lu O_3 edge is more prominent than the unmodified Lu O_2 edge, but the opposite is true for the modified versions.

The valence band density-of-states (DOS) used for LSO (Figure 42) is taken from a density functional theory (DFT) calculation by [51]. The sharp peak in the middle of the valence band appears to be due to the lutetium 4f states, though [51] states that this occurs between -5 and -7 eV, presumably relative to the valence band maximum. Since the DOS is in units of electrons/eV, the peak can be integrated to confirm that it is consistent with 14 states due the Lu-4f orbital. Multiplying 14 4f electrons per Lu, by 2 Lu atoms per LSO molecule, by 8 molecules in the unit cell (Figure 43) gives 224 electrons. Integrating the region of the DOS in the neighborhood the peak gives ~250, which is as close as one could expect to be considering that the 4f peak is superimposed on other valence band states. Aside from Lu-4f, the rest of the valence band is primarily due to oxygen 2p electrons. The feature at the bottom of the valence band shown by the dashed curve in Figure 42 is not included by [51] and is calculated with VASP as

with the other compounds. The IMFP for the components of the inelastic electron

scattering model is shown in Figure 44.
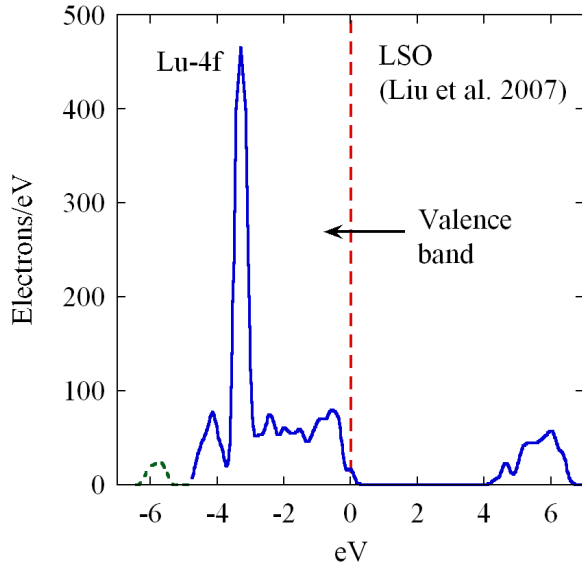
Figure 42. Density-of-states for LSO from Liu et al. (2007). As is the case with DFT calculations, the bandgap is underestimated. The dashed part of the curve around -6 eV was calculated using VASP.
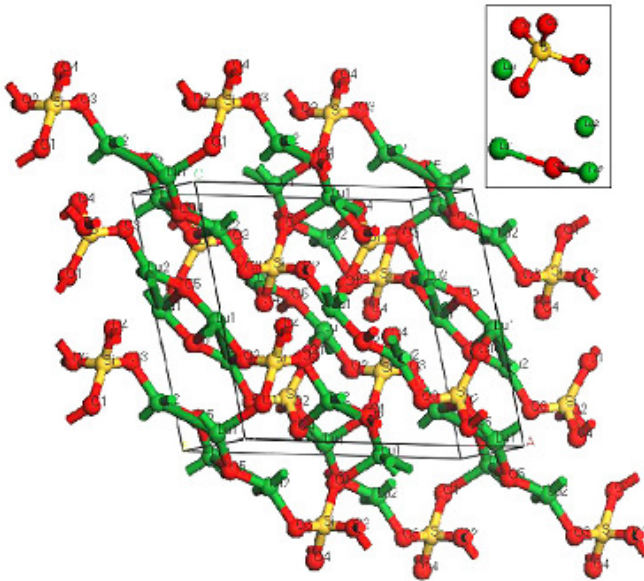
Figure 43. Illustration from Liu et al. (2007) of the unit cell (enclosed by the black lines) used for the calculation of the density of states surrounding the bandgap in LSO. Lutetium atoms are colored green, silicon yellow, and oxygen red. There are 8 LSO molecules in the unit cell.
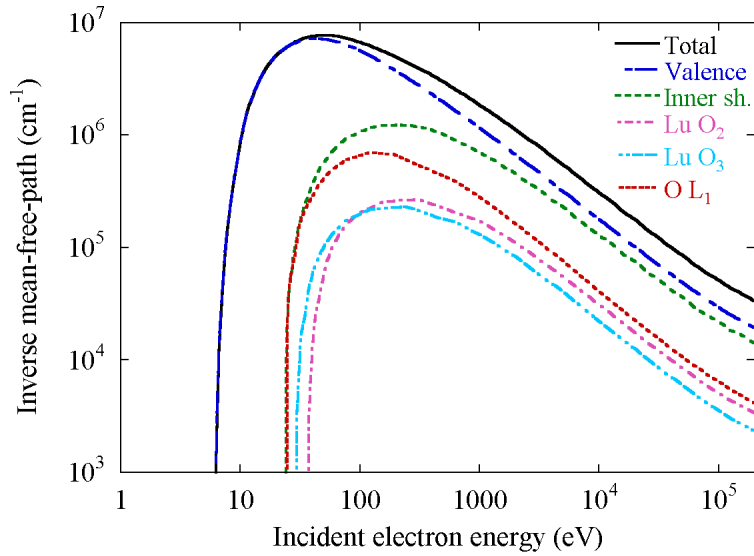
Figure 44. Model inverse mean-free-path for LSO.

A histogram of the simulated response of LSO to 200 keV gamma-rays is shown in Figure 45, and the higher-energy portion with smaller bins in Figure 46. As with CeF$_3$, the Compton edge is present at ~88 keV. The cylindrical geometry has a radius of 3 cm and height 6 cm. This simulation gives $w = 9.91\,\text{eV}$ and $F = 0.066$.
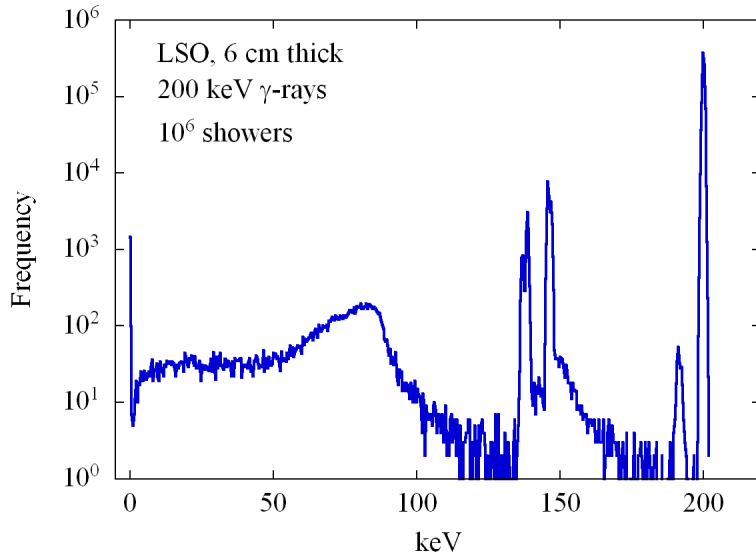
Figure 45. Simulated response of LSO to 200 keV gamma-rays. The detector geometry consists of a cylinder with a diameter and height of 6 cm.
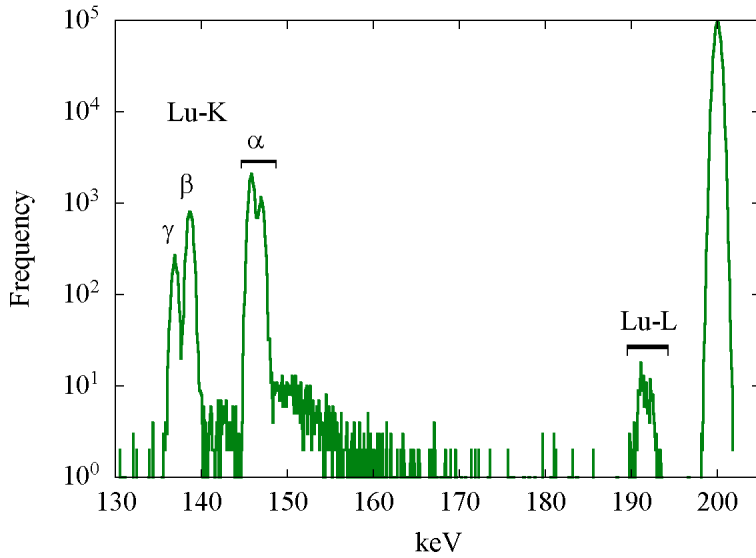
Figure 46. Photopeak (full energy deposition) and escape peaks for LSO.

94

7   Discussion

Input parameters and results for the five simulated detector materials are listed in

Table 3. For the scintillators CeF_3 and LSO plasmon excitation was not included

and the valence excitation component was taken directly from the EELS spectra,

so most parameters are not applicable. In addition to F and w, the product Fw is

shown since this, not F, is proportional to the square of the intrinsic energy

resolution (the FWHM of the full-energy peak is $2.355 \times \sqrt{FwE_0}$). In this chapter

results are explained in the context of the electron cascade, and that is followed by

further discussion of the issue of the appropriate effective bandgap and w which

was initiated in §4.9.2 for silicon.

Table 3

Parameters and results for simulated materials

| Input/Result	Symbol	Si	GaAs	ZnTe	CeF₃	LSO
Plasmon resonance energy	E_P	16.7	15.5	17.35	——	——
Plasmon decay constant	$\Delta E_P \equiv \hbar\Gamma$	3.7	7.74	9.0	——	——
Plasmon dispersion coefficient	α	2	2	2	——	——
Fermi energy	E_F	12.78	11.5	10.2	——	——
Valence excitation peak	ΔU_{peak}	2.5	2.5	1.84	——	——
Valence excitation "tail" parameter	B	0.1	0.3	0.124	——	——
Plasmon to valence excitation ratio.	W_P	0.7	0.6	0.893	——	——
Optical phonon energy	$\hbar\omega_{opt}$	0.05	0.0364	0.025	——	——
Integral of optical phonon energy-loss function	$\hbar I$	6.6e-6	8.08e-4	2.2e-3	——	——
Effective bandgap	E_G	2.3	2.4	3.8	8	6

Input/Result	Symbol	Si	GaAs	ZnTe	CeF$_3$	LSO
Valence band width	E_v	10.88	6.698	5.225	3.281	6.413
Average pair energy	w	3.66	4.144	6.317	11.59	9.909
Fano factor	F	0.091	0.100	0.075	0.046	0.066
Product of above	Fw	0.333	0.412	0.473	0.537	0.650

7.1 Predicting intrinsic energy resolution

Results for F (Figure 47) and w (Figure 48) are plotted for the five simulated

materials along with the "toy model" from §4.9.1 where both a uniform valence

band density-of-states and a uniform inelastic electron scattering differential cross

section (or differential IMFP) are assumed. It is not surprising that results for the

materials differ substantially from the simplistic toy model, since this was the

case for silicon in §4.9.2. The Fano factor for silicon is reduced from 0.091 to

0.079 when the valence band DOS shown in Figure 17 is replaced with a uniform

DOS, and w is reduced by 0.09 eV (0.04 on the scale of Figure 48). This brings F

and w considerably closer to the curves for the "toy model," providing evidence

for the significance of the valence band structure. The low Fano factor and pair

energy for CeF$_3$ are consistent with the observation from §4.9.1 regarding the

distribution of electrons and holes at the end of the cascade. Results plotted for Si

and GaAs are for 10 keV electrons rather than gamma-rays, since this makes little

or no difference in the determination of F and w. For the remaining materials

results for 200 keV gamma-rays are plotted, since for these materials F and w

appear to be different when the simulation begins with a gamma-ray.
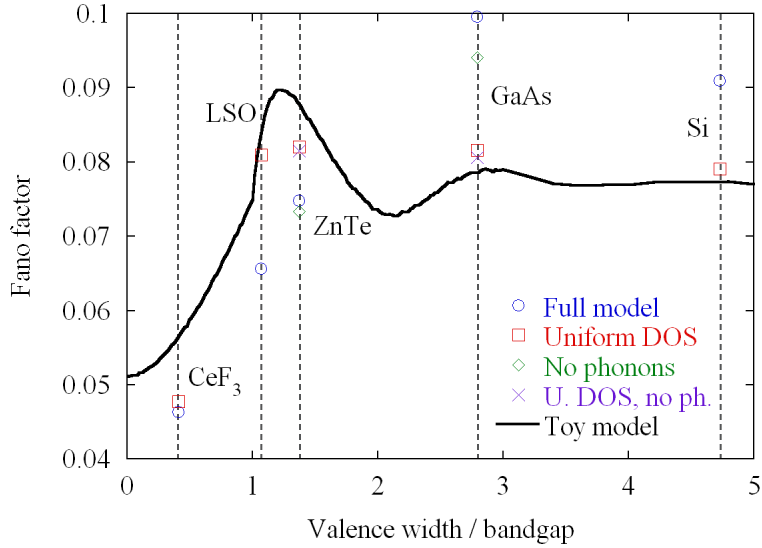
Figure 47. Fano factor for simulated materials against the ratio of valence band width to effective bandgap. Fano factors are also shown for the case where the valence band DOS is replaced by a uniform DOS of the same width, and results for GaAs and ZnTe are shown with and without phonon scattering.

Figure 48. Average electron-hole pair energy for simulated materials against the ratio of valence band width to effective bandgap. Pair energies also shown for the case where the valence band DOS is replaced by a uniform DOS of the same width, and results for GaAs and ZnTe are shown with and without phonon scattering.
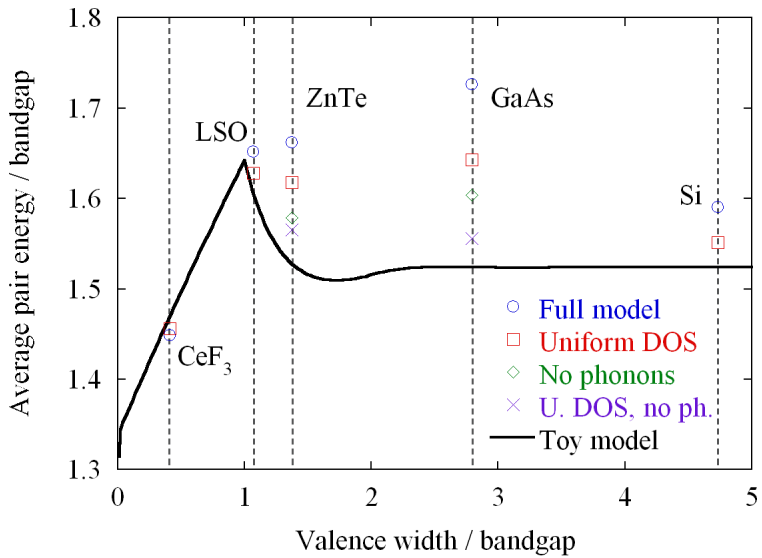
For the compound semiconductors Figure 47 and Figure 48 also include

the effects of phonons. Phonon emission (absorption is not simulated) causes

electrons to lose energy without creating additional electron-hole pairs. When phonon emission causes an electron's kinetic energy to fall below the ionization threshold, which is equal to the effective bandgap in these simulations, the creation of an additional electron-hole pair is prevented. This should have the effect of raising w, and indeed w is reduced when phonons are excluded from the simulation (Figure 48). One expects that any random process that removes energy without creating electron-hole pairs should be detrimental to energy resolution, and this occurs in the simulations of GaAs and ZnTe. Using both the calculated and uniform valence band DOS, F is reduced when phonons are excluded. Since energy resolution deteriorates when the product Fw is increased, and both F and w are increased by phonon scattering, we conclude that phonon scattering is detrimental to energy resolution. Although the calculated effect of phonon scattering on energy resolution for GaAs and ZnTe is relatively modest, this may not be the case for compound semiconductors with narrower bandgaps. Phonon scattering is the dominant process only at the lowest energies, and materials with narrow bandgaps will have lower ionization thresholds, therefore phonon scattering will be important over a broader range of electron energies. It is probably for this reason that phonon scattering appears to have a greater effect in GaAs (effective $E_G = 2.4$ eV) than in ZnTe (effective $E_G = 3.8$ eV). Finally, phonon scattering has only been simulated for electrons, while it should also occur for holes. This means that phonon scattering may have a greater influence for materials whose valence bands have widths exceeding the effective bandgap

98

$(E_V > E_G)$. Phonon scattering of holes should not matter when $E_V < E_G$ since holes in the valence band will not be capable of causing additional pairs.

In §4.9.1 the possibility of engineering detector materials to optimize energy resolution was illustrated using a model for a generic material described by a few parameters. F is shown to oscillate with the ratio E_P/E_V (Figure 15) but this variation is only significant when the plasmon is strong compared to other inelastic processes and the peak is narrow. Also, this effect is only significant when $E_P/E_V < 3w$, so it would only be relevant for semiconductors with very wide bandgaps, as even ZnTe barely meets this criteria. Although plasmons were not incorporated in the model for the scintillators, the same effect should be observed if there is there is a sharp feature that dominates the low-loss region of the EELS spectrum. Based on values for w and the EELS spectra for the five simulated materials, it is difficult to draw any conclusions regarding the significance of the ratio E_P/E_V.

Considering Figure 47, it does appear that the width of the valence band affects the Fano factor, even when the material-specific scattering model is incorporated. Comparing F for CeF$_3$ versus LSO, the dependence of F on E_V/E_G appears to follow the toy model to a great extent. The Fano factor for CeF$_3$ is sufficiently low that the product Fw is smaller than for LSO despite the greater value of w in CeF$_3$. It is still impossible, though, for CeF$_3$ to surpass the intrinsic energy resolution of the semiconductors. As discussed in §3.2, the

contribution of Fano statistics to energy resolution in scintillators will be of little

consequence until significant advances are made in photodetectors.

7.2   Holes in the model

In the analysis of silicon in §4.9.2, the inelastic electron scattering model resulted

in a value $w \approx 1.9$ eV when the minimum bandgap 1.15 eV was used, and this

value for w is much lower than the frequently cited ~3.7. The same issue is

present for GaAs, so presumably the choice of effective bandgap is a complex

issue for many semiconductors. The true value of the average electron-hole pair

energy is critical in establishing the best possible energy resolution for a material,

so this point deserves further discussion. The focus will be on silicon, since it has

a long history of measurements in the literature.

Measurements of w in silicon are consistent with each other, as most seem

to be within a few percent of 3.7 eV[21, 66, 67]. It appears that this value is so

thoroughly accepted that some authors (for example Papp et al.[24]) cite it

without giving a reference. Interestingly, measurements of the Fano factor in

silicon vary from 0.067[24] to about twice that (see Table 1 from Fraser et al.[7]).

Since F is meant to be an intrinsic material property, and the intrinsic component

of energy resolution is determined by the product Fw, it may be that an incorrect

value has been assumed for w. That it takes 3.7 eV to produce an electron-hole

pair is rather confusing from a theoretical standpoint. According to the

calculation of Sano and Yoshii[15], even electrons in the lowest conduction band

of silicon will ionize the valence band at a rate $\sim 10^{10}$ s^{-1} when they have energies

1.15 eV from the conduction band minimum. This figure does not include

phonon-assisted processes. If electrons are collected in 10^{-8} s [18], it would then seem possible that electrons with energies barely in excess of the minimum bandgap (relative to the conduction band minimum) would still be able to ionize the valence band.

There will also be an ionization threshold for holes in the valence band, and it must be at least one bandgap's width from the top of the valence band. By analyzing the band structure of silicon, Medvedev and Rethfeld[68] determine that holes must be lower in the valence band then 3 eV from the conduction band minimum in order to create an additional electron-hole pair by impact ionization, conserving both energy and momentum. These authors give a threshold for electrons of 1.2 eV (from the conduction band minimum). Again, this does not consider phonon assisted processes. Using these thresholds they calculate $w = 2.62$ eV (they call it an *effective energy-gap*) for ultrashort laser pulses of 38 eV photons. The lower incident energy may make a modest difference in w, but the short (~25 femtoseconds) timescale simulated should only make w greater than it would be in the radiation detector case since electrons and holes will have less time to relax towards the bandgap.

Medvedev and Rethfeld[68] then make a very interesting assertion. They state that their *effective energy-gap* cannot be compared to measurements of the average pair energy w because the latter occur on a timescale where the recombination of electrons and holes is important. If electrons low in the conduction band and holes toward the top of the valence band recombine then w will be increased. Electron-hole recombination should depend on the physical

dimensions and bias voltage of the detector, so it would arguably be counted in terms of incomplete charge collection rather than intrinsic resolution in equation (3.19). That recombination would have the effect of increasing the apparent value of w in measurements seems contradictory to the quoted carrier lifetime of $\sim 10^{-3}$ s [25] in silicon. A study of the electron cascade which takes into account both energy and momentum conservation within the band structure, in addition to phonon-assisted processes and the carrier collection process, may be required to understand whether recombination explains the measured value of w.

8 Conclusion

In this dissertation a model has been developed for calculating in both scintillation and semiconductor gamma-ray detectors the component of the energy resolution due to the statistics of electron-hole pair production. A physical model for inelastic electron scattering, which utilizes data from electron energy-loss spectroscopy (EELS), is developed in §4 which calculates the number of electron-hole pairs produced in a cascade initialed by a fast electron. Results are obtained for a generic material to investigate the dependence of energy resolution on material properties. Energy resolution, in terms of the Fano factor, is shown to vary with the ratio of both plasmon energy and valence band width to the bandgap. The electron scattering model is also applied to silicon. Results for cascades initiated by a fast electron are to a great extent relevant for the gamma-ray case.

This model for inelastic electron scattering is incorporated in the Penelope radiation transport code[16] so that photon processes can also be included (§5). The full model is applied to semiconductors Si, GaAs, and ZnTe and scintillators CeF_3 and LSO (§6) and simulated detector response functions are presented. For all of these materials, results for the Fano factor and average electron-hole pair energy w are fairly close to the predictions of the toy model after the effects of the valence band density-of-states and phonon scattering are removed. This means that in many cases the details of the differential scattering cross-section for inelastic electron processes may have little effect on energy resolution. These issues may be clarified by the examination of more detector materials and more

accurate differential cross section measurements from EELS spectra taken with improved energy resolution.

One cause for concern in this work has been the discrepancy between the predicted and observed values of the average pair energy w in semiconductors. It has been suggested[68] that this could be due to electron-hole recombination, but this remains unclear. It may be necessary to run more detailed simulations for low-energy electrons and holes, which consider both energy and momentum conservation.

References

[1] R.T. Kouzes, The installation of radiological monitoring equipment in the United States and overseas is helping thwart nuclear terrorism, American Scientist, 93 (2005).

[2] C.F.G. Delaney, E.C. Finch, Radiation Detectors: Physical Principles and Applications, Clarendon Press, Oxford, 1992.

[3] U. Fano, Ionization yield of radiations: II The fluctuations of the number of ions, Phys. Rev., 72 (1947) 26-29.

[4] W. van Roosbroeck, Theory of the yield and Fano factor of electron-hole pairs generated in semiconductors by high energy particles, Phys. Rev. , 139 (1965) 1702-1716.

[5] R.C. Alig, S. Bloom, C.W. Struck, Scattering by ionization and phonon emission in semiconductors, Phys. Rev. B, 22 (1980) 5565-5582.

[6] R.C. Alig, Scattering by ionization and phonon emission in semiconductors II Monte Carlo calculations, Phys. Rev. B, 27 (1983) 968-977.

[7] G.W. Fraser, A.F. Abbey, A. Holland, K. McCarthy, A. Owens, A. Wells, The X-ray energy response of silicon: Part A Theory, Nucl. Inst. Meth., A 350 (1994) 368-378.

[8] F. Gao, L.W. Campbell, R. Devanathan, Y.L. Xie, L.R. Corrales, A.J. Peurrung, W.J. Weber, Monte Carlo method for simulating gamma-ray interaction with materials: A case study on Si, Nuc. Instr. and Meth. A, 579 (2007) 292-296.

[9] F. Gao, L.W. Campbell, R. Devanathan, Y.L. Xie, Y. Zhang, A.J. Peurrung, W.J. Weber, Gamma-ray interaction in Ge: A Monte Carlo simulation, Nuc. Instr. and Meth. B, 255 (2007) 286-290.

[10] R. Devanathan, L.R. Corrales, F. Gao, W.J. Weber, Signal variance in gamma-ray detectors - A review, Nucl. Inst. and Meth. A, 565 (2006) 637-649.

[11] D.V. Jordan, A.S. Renholds, J.E. Jaffe, K.K. Anderson, L.R. Corrales, A.J. Peurrung, Simple classical model for Fano statistics in radiation detectors, Nucl. Inst. and Meth. A, 585 (2008) 146-154.

[12] C. Caleman, C. Ortiz, E. Marklund, F. Bultmark, M. Gabrysch, F.G. Parak, J. Hajdu, M. Klintenberg, N. Timneanu, Radiation damage in biological material: Electronic properties and electron impact ionization in urea (vol 85, 18005, 2009), A Letters J. Expl. the Front. of Phys., 88 (2009).

[13] C. Ortiz, C. Caleman, Secondary electron cascade dynamics in KI and CsI, J. Phys. Chem. C, 111 (2007) 17442-17447.

[14] E.O. Kane, Electron Scattering by Pair Production in Silicon, Phys. Rev., 159 (3) (1967) 624-631.

[15] N. Sano, A. Yoshii, Impact-ionization theory consistent with a realistic band structure of silicon, Phys. Rev. B, 45 (1992) 4171.

[16] J. Baró, J. Sempau, J.M. Fernández-Varea, F. Salvat, PENELOPE: An algorithm for Monte Carlo simulation of the penetration and energy loss of electrons and positrons in matter, Nucl. Inst. and Meth. B, 100 (1995) 31-46.

[17] P.N. Cooper, Introduction to Nuclear Radiation Detectors, Cambridge University Press, Cambridge, 1986.

[18] G.F. Knoll, Radiation Detection and Measurement, 3rd ed., Wiley, New York, 2000.

[19] C. Kittel, P. McEuen, Introduction to Solid State Physics, 8th ed., J. Wiley, Hoboken, NJ, 2005.

[20] Y. Bar-Shalom, X.-R. Li, T. Kirubarajan, Estimation with applications to tracking and navigation, Wiley, New York, 2001.

[21] B.G. Lowe, R.A. Sareen, A measurement of the electron-hole pair creation energy and the Fano factor in silicon for 5.9 keV X-rays and their temperature dependence in the range 80-270 K, Nuc. Instr. and Meth. A, 576 (2007) 367-370.

[22] A. Owens, G.W. Fraser, K.J. McCarthy, On the experimental determination of the Fano factor in Si at soft X-ray wavelengths, Nucl. Inst. and Meth. A, 491 (2002) 437-443.

[23] F. Perotti, C. Fiorini, Observed energy dependence of Fano factor in silicon at hard X-ray energies, Nucl. Inst. and Meth. A, 423 (1999) 356-363.

[24] T. Papp, M.C. Lepy, J. Plagnard, G. Kalinka, E. Papp-Szabo, A new approach to the determinaiton of the Fano factor for semiconductor detectors, X-ray Spectrom., 34 (2005) 106-111.

[25] A. Owens, A. Peacock, Compound semiconductor radiation detectors, Nucl. Inst. and Meth. A, 531 (2004) 18-37.

[26] A. Owens, Spectral degradation effects in an 86 cm3 Ge(HP) detector, Nucl. Inst. and Meth. A, 238 (1985) 473-478.

[27] C.C. Ahn, O.L. Krivanek, EELS Atlas, Gatan, Inc. and ASU, Pleasanton, Ca, 1983.

[28] H.M. Rosenberg, The Solid State: An Introduction to the Physics of Solids for Students of Physics, Materials Science, and Engineering, 3rd ed., Oxford University Press, Oxford Oxfordshire ; New York, 1992.

[29] F. Salvat, J.M. Fernández-Varea, J. Sempau, PENELOPE, a code system for Monte Carlo simulation of electron and photon transport, Universitat de Barcelona, Barcelona, 2003.

[30] D.E. Cullen, S.T. Perkins, S.M. Seltzer, Photon and Electron Data-Bases and Their Use in Radiation Transport Calculations, Appl. Rad. and Iso., 44 (1993) 1343-1347.

[31] H. Raether, Excitation of Plasmons and Interband Transitions by Electrons, Springer-Verlag, Berlin ; New York, 1980.

[32] R.F. Egerton, Electron Energy Loss Spectroscopy in the Electron Microscope, Plenum, New York, 1986.

[33] R.H. Ritchie, A. Howie, Electron excitation and the optical potential in electron microscopy, Phil. Mag., 36 (1977) 463-481.

[34] W.H. Press, W.T. Vetterling, Numerical recipes in FORTRAN : the art of scientific computing, 2nd ed., Cambridge University Press, Cambridge, 1992.

[35] M.S. Chung, T.E. Everhart, Role of Plasmon Decay in Secondary-Electron Emission in Nearly-Free-Electron Metals - Application to Aluminum, Phys. Rev. B, 15 (1977) 4699-4715.

[36] P. Rez, Accurate Cross Sections for Microanalysis, J. Res. Natl. Inst. Stand. Technol., 107 (2002) 487-495.

[37] G. Kresse, J. Furthmüller, Efficient iterative schemes for ab initio total-energy calculations using a plane-wave basis set, Phys. Rev. B, 54 (1996) 11169.

[38] G. Kresse, J. Furthmüller, Efficiency of ab-initio total energy calculations for metals and semiconductors using a plane-wave basis set, Comp. Mat. Sci., 6 (1996) 15-50.

[39] B. Ziaja, R.A. London, J. Hajdu, Unified Model of Secondary Electron Cascades in Diamond, J. Appl. Phys., 97 (2005).

[40] Matlab, in, The Mathworks, 2007.

[41] D. Bote, F. Salvat, A. Jablonski, C.J. Powell, Cross sections for ionization of K, L and M shells of atoms by impact of electrons and positrons with energies up to 1 GeV: Analytical formulas, At. Data and Nucl. Data Tab., 95 (2009) 871-909.

[42] C.J. Powell, Cross Sections for Ionization of Inner-Shell Electrons by Electrons, Rev. Mod. Phys., 48 (1976) 33-46.

[43] W.E. Drummond, J.L. Moll, Hot Carriers in Si and Ge Radiation Detectors, J. Appl. Phys., 42 (1971) 5556-5562.

[44] E.D. Palik, G. Ghosh, Handbook of optical constants of solids, Academic Press, Orlando, 1985.

[45] L.C. Emerson, R.D. Birkhoff, V.E. Anderson, R.H. Ritchie, Electron Slowing-Down Spectrum in Irradiated Silicon, Phys. Rev. B, 7 (1973) 1798.

[46] D.J. Bartelink, J.L. Moll, N.I. Meyer, Hot-Electron Emission From Shallow p-n Junctions is Silicon, Phys. Rev., 130 (1963) 972.

[47] J.M. Maclaren, S. Crampin, D.D. Vvedensky, R.C. Albers, J.B. Pendry, Layer Korringa-Kohn-Rostoker electronic structure code for bulk and interface geometries, Comp. Phys. Commun., 60 (1990) 365-389.

[48] M.N. Mazziotta, Electron-hole pair creation energy and Fano factor temperature dependence in silicon, Nucl. Inst. and Meth. A, 584 (2008) 436-439.

[49] W. Heitler, The quantum theory of radiation, 3d ed., Clarendon Press, Oxford,, 1954.

[50] G.B. Rybicki, A.P. Lightman, Radiative Processes in Astrophysics, WILEY-VCH, Weinheim, 2004.

[51] B. Liu, Z. Qi, M. Gu, X. Liu, S. Huang, C. Ni, First-principles study of oxygen vacancies in Lu_2SiO_5, J. Phys.: Condens. Matter, 19 (2007) 436215.

[52] K. Siegbahn, V.-s.i. Upsala, ESCA; atomic, molecular and solid state structure studied by means of electron spectroscopy, Almqvist & Wiksells, Uppsala, 1967.

[53] U. Schötzig, Half-life and X-ray emission probabilities of ^{55}Fe, Appl. Rad. and Iso., 53 (2000) 469-472.

[54] A. Owens, A. Peacock, M. Bavdaz, Progress in Compound Semiconductors, in: Proc. SPIE, 2003, pp. 1059.

[55] A. Owens, M. Bavdaz, A. Peacock, A. Poelaert, H. Andersson, S. Nenonen, H. Sipila, L. Tröger, G. Bertuccio, High resolution X-ray spectroscopy using GaAs arrays, J. Appl. Phys., 90 (2001) 5376–5381.

[56] G. Bertuccio, A. Pullia, J. Lauter, A. Forster, H. Luth, Pixel X-ray detectors in epitaxial gallium arsenide with high-energy resolution capabilities (Fano factor experimental determination), IEEE Trans. Nucl. Sci., 44 (1997) 1-5.

[57] D.J. Olego, J.P. Faurie, S. Sivananthan, P.M. Raccah, Optoelectronic properties of $Cd_{1-x}Zn_xTe$ films grown by molecular beam epitaxy on GaAs substrates, Appl. Phys. Lett., 47 (1985) 1172-1174.

[58] K. Klier, P. Novák, A.C. Miller, J.A. Spirko, M.K. Hatalis, Electronic structure of CeF3 and TbF3 by valence-band XPS and theory, Journal of Physics and Chemistry of Solids, 70 (2009) 1302-1311.

[59] K. Wei, C. Guo, J. Deng, C. Shi, Electronic structure of CeF_3 crystal, J. Electron Spectrosc. Relat. Phenom., 79 (1996) 83-85.

[60] M. Nisar, A. Roth, G. Stephan, S. Robin, Far ultraviolet reflectance spectra of CeF_3, PrF_3 and NdF_3, Optics Commun., 8 (1973) 254-256.

[61] I. Valais, S. David, C. Michail, A. Konstantinidis, I. Kandarakis, G.S. Panayiotakis, Investigation of luminescent properties of LSO:Ce, LYSO:Ce and GSO:Ce crystal scintillators under low-energy gamma-ray excitation used in nuclear imaging, Nucl. Inst. and Meth. A, 581 (2007) 99-102.

[62] W.W. Moses, M. Janecek, M.A. Spurrier, P. Szupryczynski, W.S. Choong, C.L. Melcher, M. Andreaco, Optimization of a LSO-Based Detector Module for Time-of-Flight PET, IEEE Trans. Nucl. Sci., 57 (2010) 1570-1576.

[63] R.D. Leapman, P. Rez, D.F. Mayers, K, L, and M shell generalized oscillator strengths and ionization cross sections for fast electron collisions, J. Chem. Phys., 72 (1980) 1232-1243.

[64] P. Rez, Cross-sections for energy loss spectrometry, Ultramicroscopy, 9 (1982) 283-287.

[65] C.C. Ahn, P. Rez, Inner shell edge profiles in electron energy loss spectroscopy, Ultramicroscopy, 17 (1985) 105-115.

[66] R.H. Pehl, F.S. Goulding, D.A. Landis, M. Lenzlinger, Accurate determination of the ionization energy in semiconductor detectors, Nucl. Inst. and Meth., 59 (1968) 45-55.

[67] F. Scholze, H. Henneken, P. Kuschnerus, H. Rabus, M. Richter, G. Ulm, Determination of the electron-hole pair creation energy for semiconductors from the spectral responsivity of photodiodes, Nucl. Inst. and Meth. A, 439 (2000) 208-215.

[68] N. Medvedev, B. Rethfeld, Transient dynamics of the electronic subsystem of semiconductors irradiated with an ultrashort vacuum ultraviolet laser pulse, New J. Phys., 12 (2010).